NASA/TM-2003-212639

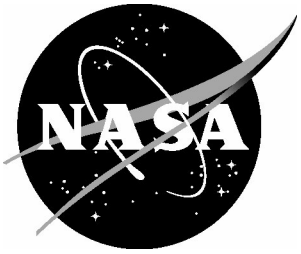

Characterization of Al-Cu-Mg-Ag Alloy RX226-T8 Plate

Cynthia L. Lach and Marcia S. Domack
Langley Research Center, Hampton, Virginia

August 2003

The NASA STI Program Office . . . in Profile

Since its founding, NASA has been dedicated to the advancement of aeronautics and space science. The NASA Scientific and Technical Information (STI) Program Office plays a key part in helping NASA maintain this important role.

The NASA STI Program Office is operated by Langley Research Center, the lead center for NASA's scientific and technical information. The NASA STI Program Office provides access to the NASA STI Database, the largest collection of aeronautical and space science STI in the world. The Program Office is also NASA's institutional mechanism for disseminating the results of its research and development activities. These results are published by NASA in the NASA STI Report Series, which includes the following report types:

- TECHNICAL PUBLICATION. Reports of completed research or a major significant phase of research that present the results of NASA programs and include extensive data or theoretical analysis. Includes compilations of significant scientific and technical data and information deemed to be of continuing reference value. NASA counterpart of peer-reviewed formal professional papers, but having less stringent limitations on manuscript length and extent of graphic presentations.

- TECHNICAL MEMORANDUM. Scientific and technical findings that are preliminary or of specialized interest, e.g., quick release reports, working papers, and bibliographies that contain minimal annotation. Does not contain extensive analysis.

- CONTRACTOR REPORT. Scientific and technical findings by NASA-sponsored contractors and grantees.

- CONFERENCE PUBLICATION. Collected papers from scientific and technical conferences, symposia, seminars, or other meetings sponsored or co-sponsored by NASA.

- SPECIAL PUBLICATION. Scientific, technical, or historical information from NASA programs, projects, and missions, often concerned with subjects having substantial public interest.

- TECHNICAL TRANSLATION. English-language translations of foreign scientific and technical material pertinent to NASA's mission.

Specialized services that complement the STI Program Office's diverse offerings include creating custom thesauri, building customized databases, organizing and publishing research results ... even providing videos.

For more information about the NASA STI Program Office, see the following:

- Access the NASA STI Program Home Page at ***http://www.sti.nasa.gov***

- E-mail your question via the Internet to help@sti.nasa.gov

- Fax your question to the NASA STI Help Desk at (301) 621-0134

- Phone the NASA STI Help Desk at (301) 621-0390

- Write to:
  NASA STI Help Desk
  NASA Center for AeroSpace Information
  7121 Standard Drive
  Hanover, MD 21076-1320

NASA/TM-2003-212639

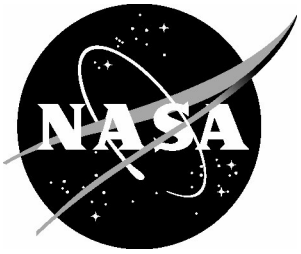

Characterization of Al-Cu-Mg-Ag Alloy RX226-T8 Plate

Cynthia L. Lach and Marcia S. Domack
Langley Research Center, Hampton, Virginia

National Aeronautics and
Space Administration

Langley Research Center
Hampton, Virginia 23681-2199

August 2003

Available from:

NASA Center for AeroSpace Information (CASI)
7121 Standard Drive
Hanover, MD 21076-1320
(301) 621-0390

National Technical Information Service (NTIS)
5285 Port Royal Road
Springfield, VA 22161-2171
(703) 605-6000

Abstract

Aluminum-copper-magnesium-silver (Al-Cu-Mg-Ag) alloys that were developed for thermal stability also offer attractive ambient temperature strength-toughness combinations, and therefore, can be considered for a broad range of airframe structural applications. The current study evaluated Al-Cu-Mg-Ag alloy RX226-T8 in plate gages and compared performance with sheet gage alloys of similar composition.

Uniaxial tensile properties, plane strain initiation fracture toughness, and plane stress tearing resistance of RX226-T8 were examined at ambient temperature as a function of orientation and thickness location in the plate. Properties were measured near the surface and at the mid-plane of the plate. Tensile strengths were essentially isotropic, with variations in yield and ultimate tensile strengths of less than 2% as a function of orientation and through-thickness location. However, ductility varied by more than 15% with orientation. Fracture toughness was generally higher at the mid-plane and greater for the L-T orientation, although the differences were small near the surface of the plate.

Metallurgical analysis indicated that the microstructure was primarily recrystallized with weak texture and was uniform through the plate with the exception of a fine-grained layer near the surface of the plate. Scanning electron microscope analysis revealed Al-Cu-Mg second phase particles which varied in composition and were primarily located on grain boundaries parallel to the rolling direction. Fractography of toughness specimens for both plate locations and orientations revealed that fracture occurred predominantly by transgranular microvoid coalescence.

Introduction

High-strength, low-density Al-Cu-Mg-Ag alloys were initially developed to replace conventional 2000 (Al-Cu-Mg) and 7000 (Al-Zn-Cu-Mg) series aluminum alloys for aircraft structural applications [1]. During the High Speed Civil Transport (HSCT) program, improvements in thermal stability were demonstrated for candidate aircraft wing and fuselage skin materials through the addition of silver to Al-Cu-Mg alloys based on Al 2519 chemistry [2]. Thermal stability of the resulting Al-Cu-Mg-Ag alloys, C415-T8 and C416-T8, was due to co-precipitation of the thermally stable Ω (AlCu) and θ' (Al_2Cu) strengthening phases [1-4]. The strength and toughness behavior was investigated for these alloys produced as 0.090-inch thick rolled sheet in the T8 condition and after various thermal exposures. The mechanical properties were shown to be competitive with conventional aircraft alloys, 2519-T8 and 2618-T8 [2]. During the Integral Airframe Structure (IAS) program, advanced aluminum alloys were examined for use in an integrally stiffened airframe structure where the skin and stiffeners would be machined from plate and extruded frames would be mechanically attached (see Figure 1) [5]. Advantages of integrally stiffened structure include reduced part count, and reduced assembly times compared to conventional built-up airframe structure. The near-surface properties of a thick plate are of significance for a machined integrally stiffened airframe structure since this represents the skin location. Properties measured at the mid-plane of the plate are more representative of the stiffener web.

RX226 was developed to exploit strength-toughness improvements and thermal stability benefits of Al-Cu-Mg-Ag alloys in plate gages. This study evaluated the microstructure and properties of three gages of plate produced in the T8 condition. Uniformity of strength and

toughness were evaluated with orientation and thickness location. Sheet gage material segments were machined at the mid-plane and near-surface locations of the plate to facilitate comparison with prior sheet products.

Objectives

The overall objective of this research was to evaluate the potential application of RX226-T8 plate for integrally stiffened airframe structure. The specific objectives included:

1) Assessment of the mechanical properties of sheet gage material machined from RX226-T8 plate for comparison with properties of Al-Cu-Mg-Ag alloys developed for sheet.
2) Characterization of the variations in tensile properties and fracture toughness of RX226-T8 plate with orientation and thickness location.
3) Characterization of the microstructure and determination of the degree of microstructural homogeneity of the plate.
4) Correlation of the observed mechanical property trends with microstructure and fracture morphology.

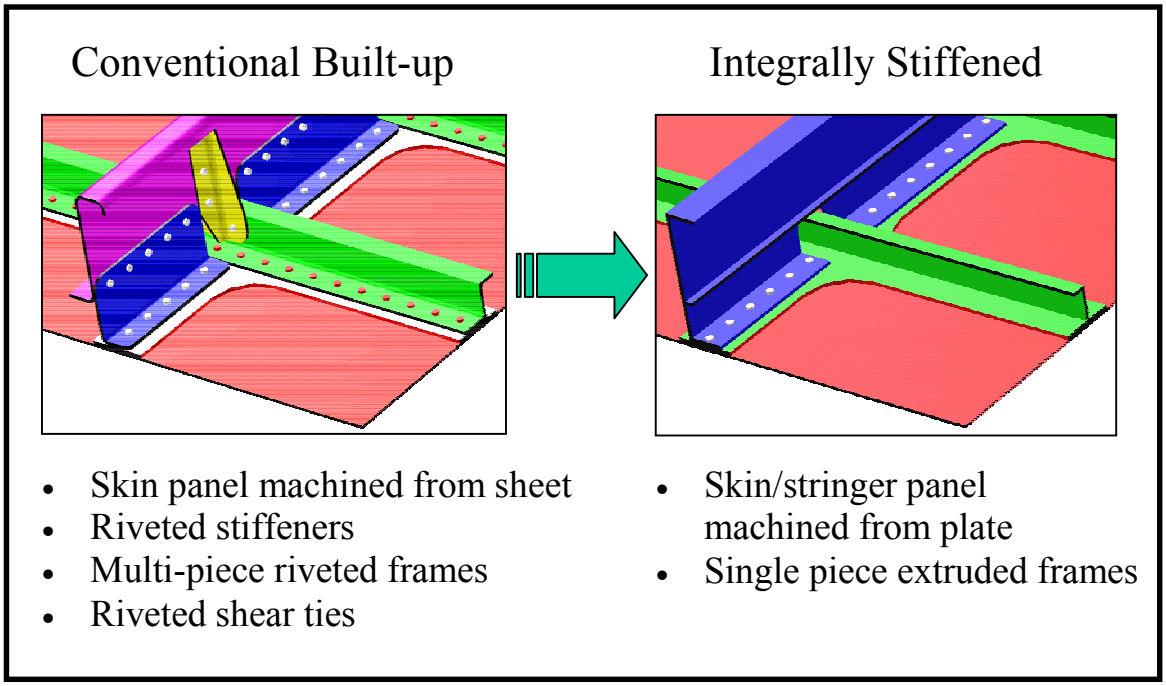

Figure 1. Built-up versus integrally stiffened airframe structural concepts [5].

Experimental Procedures

Materials

The Al-Cu-Mg-Ag alloy, RX226-T8, was produced from 1000-pound laboratory scale ingots as 1.5-inch, 1.0-inch and 0.5-inch thick rolled plates. The plates were solution heat treated at 970°F for 2 1/2 hours, cold water quenched, nominally stretched to 2.5%, and aged at 350°F

for 12 hours to the T8 condition. The actual compositions of the RX226-T8 plates are given in weight percent in Table 1. The actual compositions of the C415 and C416 evaluated during the HSCT program are included for comparison in Table 1. C415 and C416 were aged at 325°F for 16 and 36 hours, respectively, to the T8 condition.

Microstructural and mechanical property evaluations were conducted on 0.090-inch thick specimens machined from the mid-plane and near-surface plate locations to examine the properties of sheet machined from plate. The near-surface location corresponds to t/10 in the 0.5-inch thick plate, t/20 in the 1.0-inch thick plate, and t/30 in the 1.5-inch thick plate.

Table 1. Al-Cu-Mg-Ag alloy compositions

Alloy, Product form	Actual Chemistry in weight percent (wt%)												
	Cu	Mg	Ag	Mn	Zr	Ti	Ni	V	Zn	Cr	Si	Fe	Al
RX226-T8 0.5-inch plate	4.88	.46	.34	.36	.14	.05	<.01	.13	.03	<.01	.07	.07	Bal
RX226-T8 1.0-inch plate	4.90	.54	.46	.49	.17	.01	<.01	.12	.03	<.01	.04	.06	Bal
RX226-T8 1.5-inch plate	4.88	.36	.34	.46	.13	.05	<.01	.14	.03	<.01	.08	.07	Bal
C415-T8 0.090-inch sheet [2]	4.96	.81	.48	.66	.13	.01	--	--	--	--	.05	.06	Bal
C416-T8 0.090-inch sheet [2]	5.38	.53	.52	.31	.12	.01	--	--	--	--	.05	.07	Bal

-- Not available

Characterization of Microstructure

Through-thickness characterization of grain morphology and degree of recrystallization was performed on each plate. Sections normal to the longitudinal (L), transverse (T), and short transverse (S) directions from the mid-plane and near-surface regions of each plate were mounted in epoxy, polished, anodized with Barker's reagent and examined using polarized light microscopy. Orientation distribution function (ODF) texture analysis was conducted for the near-surface and mid-plane locations of the 0.5-inch and 1.0-inch thick plates. Microstructural analysis of the second phase particles was conducted on the 1.0-inch thick plate. Sections representing the LS plane of the 1.0-inch thick plate were mounted in epoxy and mechanically polished. A scanning electron microscope (SEM) operating at an accelerating voltage of 20 kV was used to examine the particle size and distribution. Chemical analysis of the particles was conducted using a KEVEX energy dispersive spectrometry system.

Mechanical Properties

All mechanical property tests were conducted with material machined from the 1.0-inch thick plate. Tensile properties were evaluated in the L and T orientations and fracture toughness in the L-T and T-L orientations for material machined from the mid-plane and near-surface locations. All tests were conducted at ambient temperature for material in the T8 condition.

Uniaxial Tensile Tests

Uniaxial tensile tests were performed according to ASTM E8-01 [6]. Duplicate tensile tests were conducted using a closed-loop servo-hydraulic test machine at a constant crosshead speed of 0.0625 in/min. Load and displacement data were collected using a personal-computer (PC) based data acquisition system. Dog bone tensile specimens, 0.090 inch thick with geometry shown in Figure 2, were machined from the mid-plane and near-surface locations of the plates in the L and T orientations. The tensile specimen elongation was measured with back-to-back

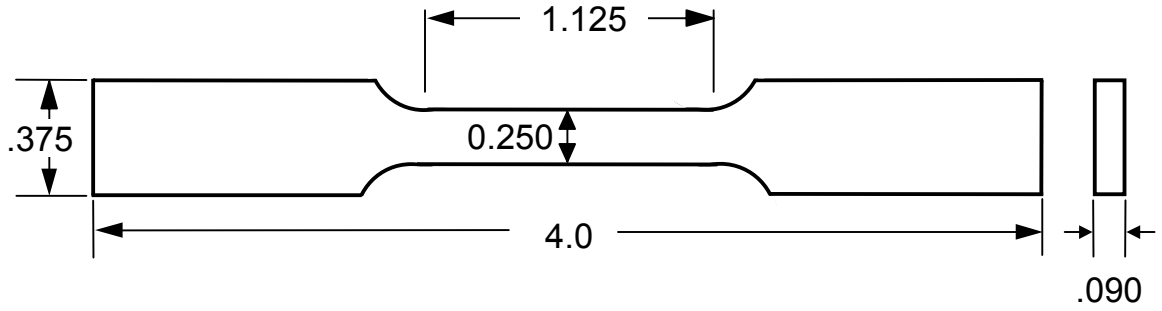

Figure 2. Dog bone tensile specimen geometry (dimensions in inches).

extensometers (1.0 inch gage length) mounted in the gage section. The load and strain data were used to determine the 0.2% offset yield strength (YS), ultimate tensile strength (UTS), and total elongation (% el) to failure. Young's modulus (E) was calculated by linear regression of the stress versus strain data from 0.001 in/in to 0.002 in/in (average of the extensometers).

Fracture Toughness Tests

Fracture toughness behavior was determined by conducting elastic-plastic J-integral fracture toughness tests that conformed to ASTM standard E1820-01 [7]. Fracture toughness and resistance to stable crack growth were determined from J-integral versus physical crack extension (Δa) curves. The effect of both orientation and plate thickness location on the fracture mode was evaluated by examining the fracture surfaces in the SEM.

Compact tension, C(T), specimens were tested using the single specimen technique with crack growth measurements made by the DC potential drop method [8-10]. The fatigue pre-cracking procedure and specimen configuration conformed to ASTM standard E1820-01 [7]. C(T) specimens (Figure 3), 0.090 inch thick (B) and 2.00 inch wide (W), were machined from the near-surface and mid-plane locations of the 1.0-inch thick plate in the L-T and T-L orientations. The C(T) specimens were fatigue pre-cracked at a constant stress ratio ($R = K_{min}/K_{max}$) of 0.1 using a closed-loop servo-hydraulic test machine with crack length determined by the compliance method. Pre-cracking of the C(T) specimens was terminated when the crack length to width ratio, a/W, reached approximately 0.60. At the end of the fatigue pre-crack procedure, K_{max} was approximately 10.0 ksi-in$^{1/2}$. Triplicate fracture toughness tests were performed in stroke control at a displacement rate of 0.010 in/min. A PC-based data acquisition and control system provided a programmable ramp signal to the stroke controller and recorded load and displacement continuously. The analysis software used elastic-plastic fracture toughness methods described in ASTM standard E1820-01 [7] for J analysis. The crack

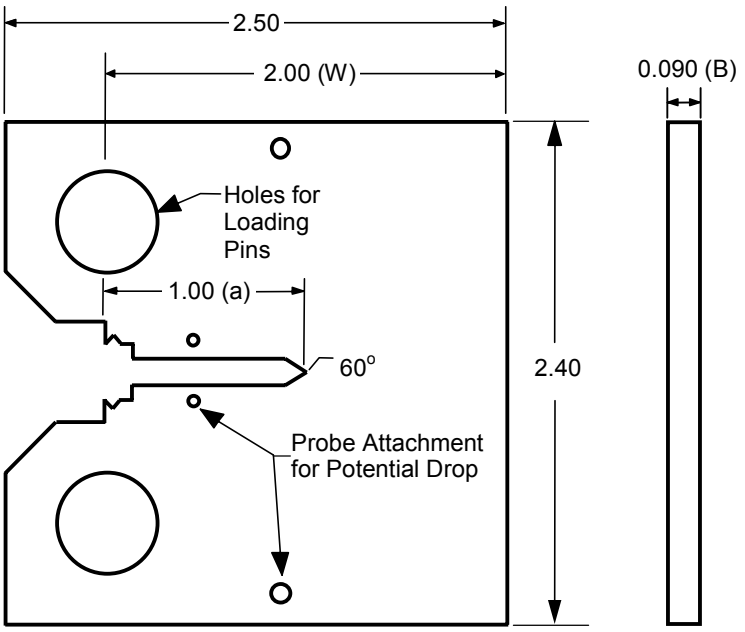

Figure 3. Fracture mechanics compact tension specimen geometry (dimensions in inches).

initiation toughness (J_{Ici}) [7] and tearing modulus (T_R) [11] were determined from the J-Δa data for each test. Plane strain fracture toughness (K_{Ici}) was calculated from [7]:

$$K_{JIci} = \{\{J_{Ici}\, E\}/\{1-\upsilon^2\}\}^{1/2} \qquad (1)$$

where υ is Poisson's ratio. For this investigation, a value of υ=0.035 was used [12]. The plane strain validity requirements for the test require that the initial ligament (b_o) and thickness (B) dimensions of the C(T) specimen must be [7]:

$$b_o, B > 25\{J_{Ici} / \sigma_o\} \qquad (2)$$

J_{Ici} characterizes the plane strain initiation toughness of a material near the onset of stable crack extension from a pre-existing fatigue crack. The flow stress (σ_o) is defined as the average of the 0.2% offset yield strength and the ultimate tensile strength at the test temperature. The tearing modulus, a measurement of material resistance to stable crack growth, was calculated from [11]:

$$T_R = \{E / \sigma_o^2\}\{dJ / \Delta da) \qquad (3)$$

where, for this study, dJ/Δda is the average slope determined by linear regression of the J-Δa data between the 0.006-inch and 0.06-inch exclusion lines [7].

Fracture surfaces of the C(T) specimens were examined in the SEM to characterize the effect of orientation and plate thickness location on the microscopic fracture morphology. Examination was limited to the specimen mid-plane and the regions 0.005 inch ahead of the pre-crack and after 0.15 inches of crack growth.

Results and Discussion

Characterization of Microstructure

The microstructure of each thickness of RX226-T8 plate was examined by preparing through-thickness montages of the LS plane and tri-planar views at the near-surface and mid-plane locations. The montages in Figure 4 show representative microstructures from the mid-plane to the surface. Tri-planar views are shown in Figures 5 through 7. In general, the microstructure was similar for all plates and exhibited predominantly recrystallized pancake-shaped grain morphology, highly elongated in the rolling direction. Occasional residual deformation bands, as noted in Figure 5(b), were observed for all plates. The microstructure of all plates was fairly homogeneous through the thickness, as illustrated in Figure 4, and was generally symmetric about the mid-plane. A region of smaller, more equiaxed grains was observed near the surface of the 0.5-inch and 1.0-inch thick plates, as can be seen in Figure 4 and by comparison of the tri-planar views. This narrow band of small recrystallized grains is likely related to the increased amount of deformation occurring at the surfaces of the thinner plate during thermomechanical processing [13]. The depth of this surface region was approximately 0.04 inch for the 0.5-inch thick plate and 0.025 inch for the 1.0-inch thick plate. The grain size was primarily uniform throughout the 1.5-inch thick plate, as evident in Figures 4 and 7.

ODF texture analysis was conducted at the near-surface and mid-plane locations for both the 0.5-inch and 1.0-inch thick plates. In each case, the texture was very weak with the majority of the values no greater than 4 times random. The texture included weak Brass and S deformation components and weak Cube and Goss recrystallization components. For the 0.5-inch thick plate, the recrystallization components were somewhat greater at the mid-plane, and the deformation components were slightly greater at the near-surface location. For the 1.0-inch thick plate, the recrystallization components varied little with thickness location and the deformation components were somewhat greater at the near-surface location.

The microstructures of C415-T8 and C416-T8 0.090-inch thick sheet, which have compositions similar to RX226 (See Table 1), were reported to be homogenous through the sheet thickness [2, 3, 14, 15]. As shown in Figure 8, C416-T8 exhibited nearly equiaxed grain morphology, while the grain size and aspect ratio were slightly larger for C415-T8. Texture analysis of both sheet alloys revealed fully recrystallized microstructures with weak texture components. The grain morphology of the RX226-T8 plates was significantly larger and more elongated than either of the C415-T8 or C416-T8 sheets and exhibited a predominantly recrystallized grain structure.

Polished metallographic samples of the LS plane from the RX226-T8 1.0-inch thick plate were viewed in the SEM to evaluate the type and distribution of second phase particles. The backscattered image shown in Figure 9 indicates that the predominant second phase particles were 1-5 μm in diameter and were observed both in the grain interior and aligned along some grain boundaries. Grain boundary particles were typically irregularly spaced and sometimes formed particle clusters. Occasional larger (10-20 μm) second phase particles were also observed. X-ray chemical analysis conducted in the SEM indicated that these particles were generally high in Cu, Fe, Zr, Mn, and Mg, and are likely intermetallic compounds.

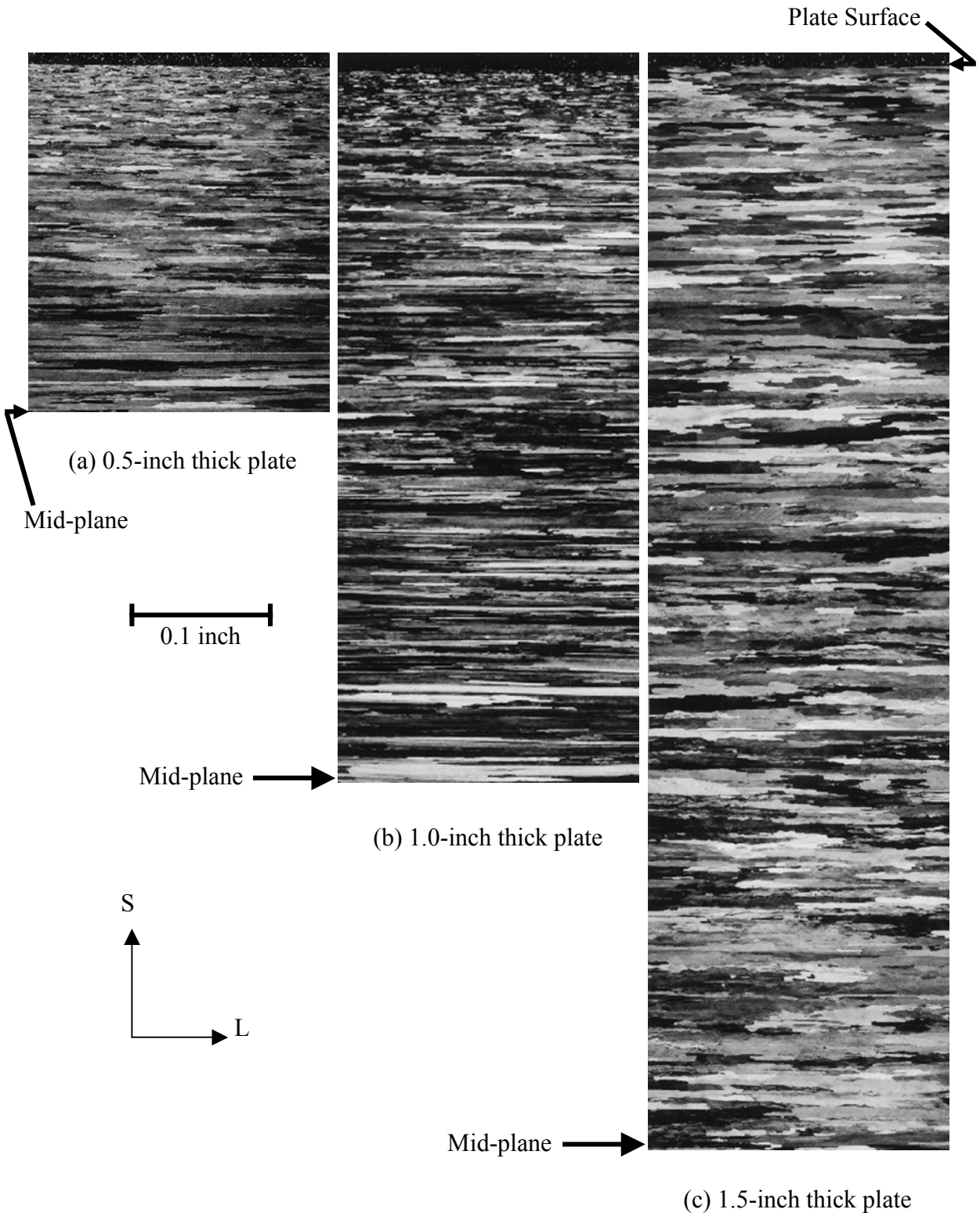

Figure 4. Microstructure of RX226-T8 plates, shown from mid-plane to surface.

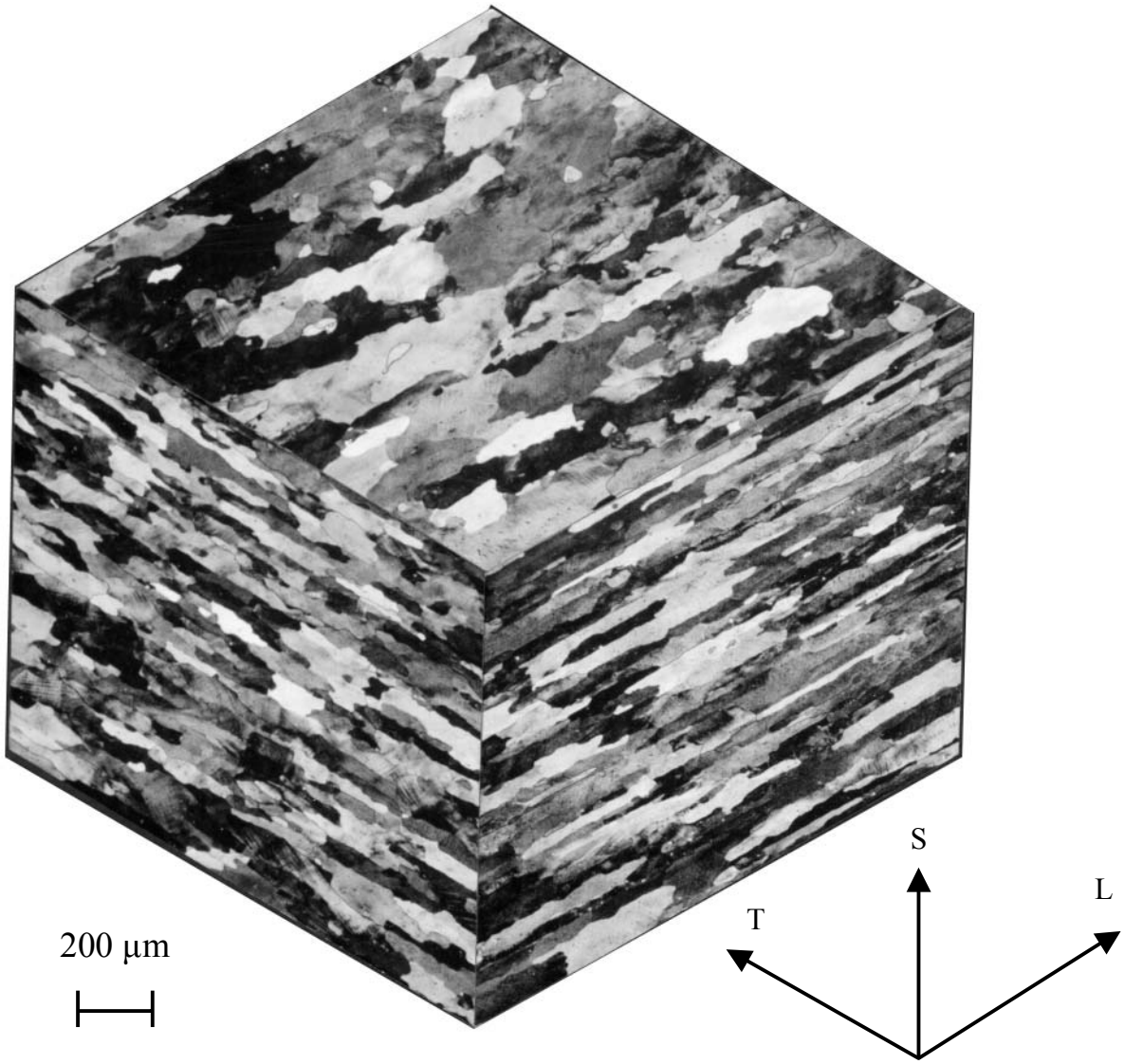

(a) Near-surface location.

Figure 5. Microstructure of RX226-T8 0.5-inch thick plate as a function of through-thickness plate location.

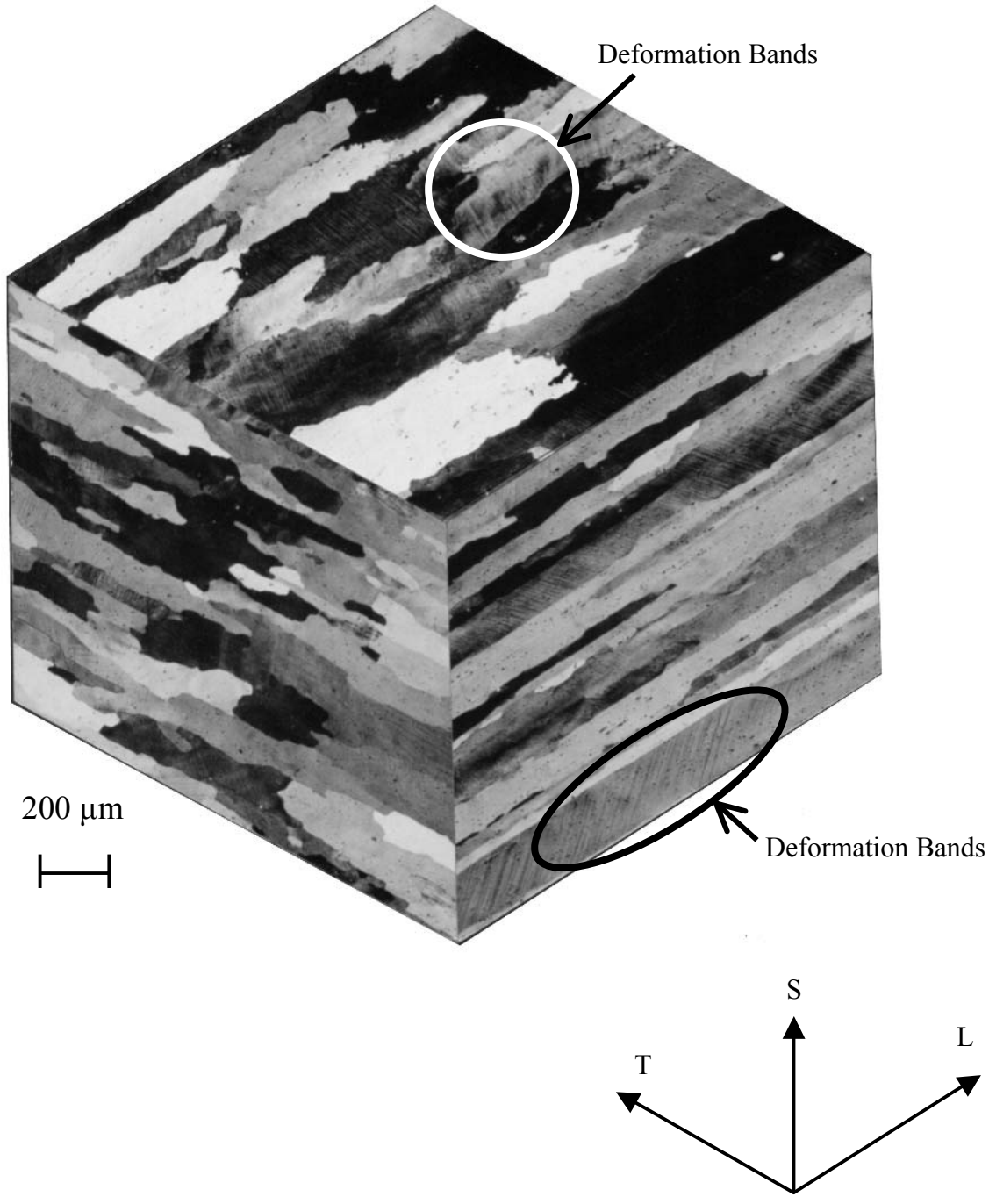

(b) Mid-plane location.

Figure 5. Concluded.

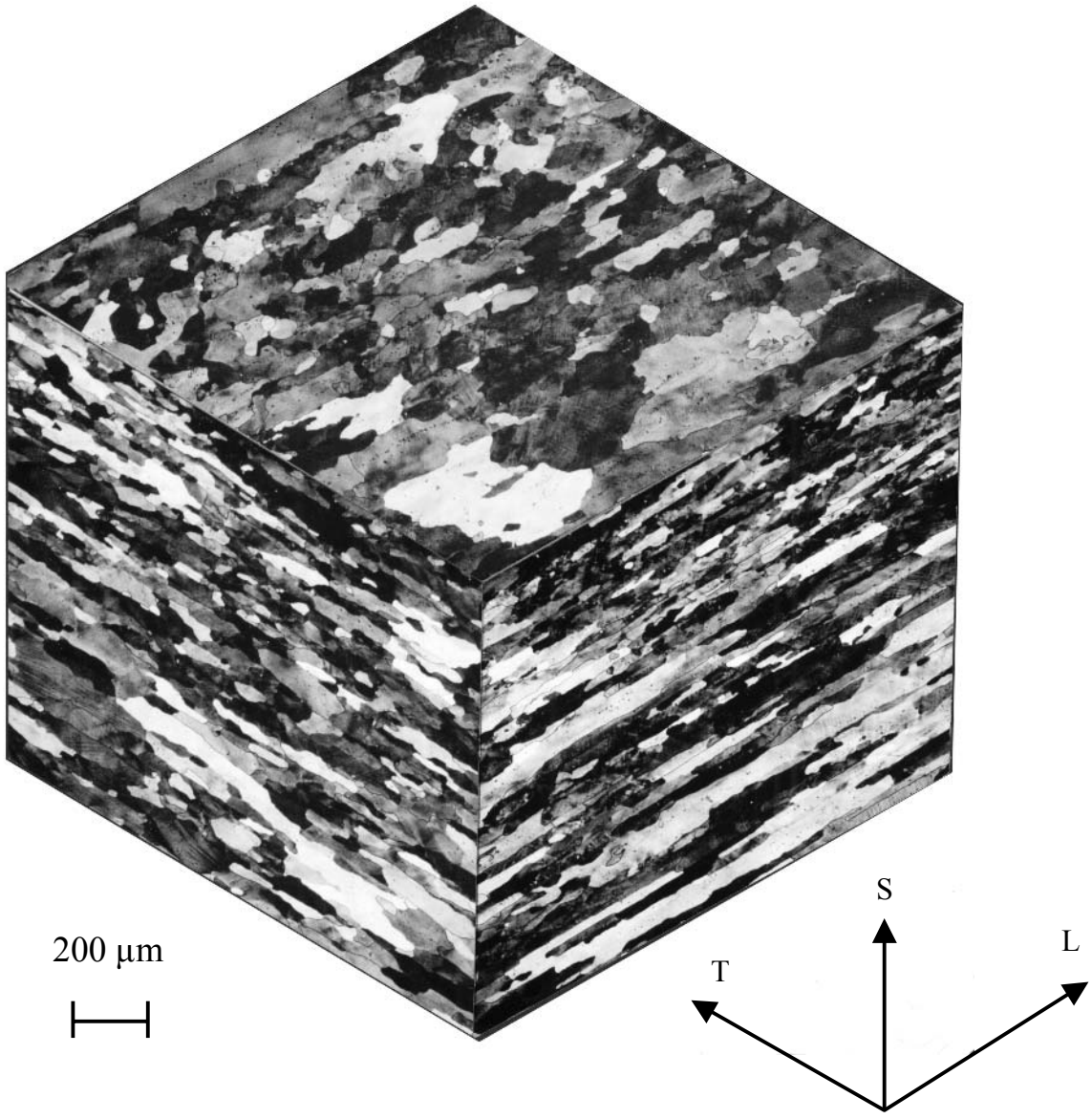

(a) Near-surface location.

Figure 6. Microstructure of RX226-T8 1.0-inch thick plate as a function of through-thickness plate location.

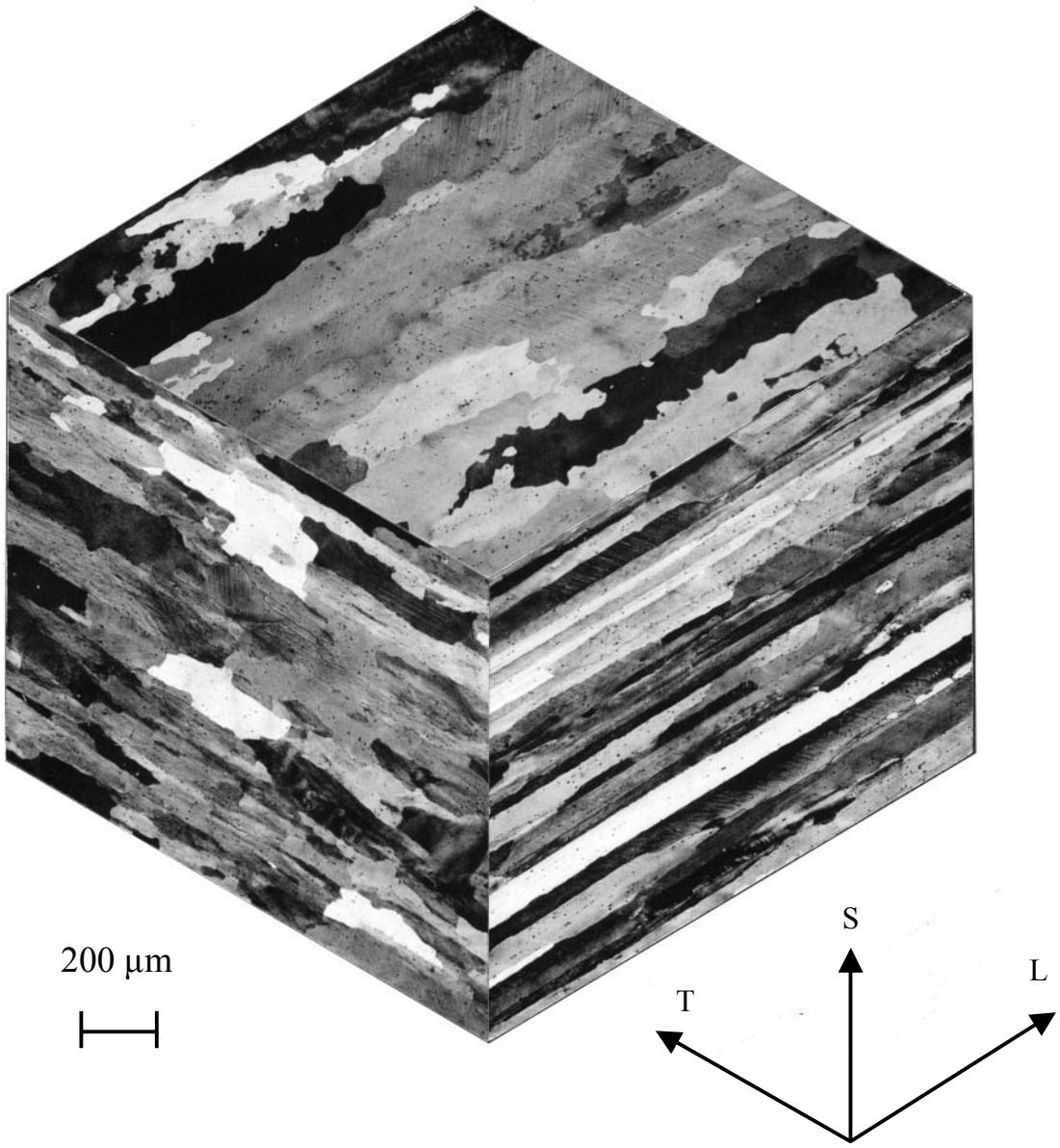

(b) Mid-plane location

Figure 6. Concluded.

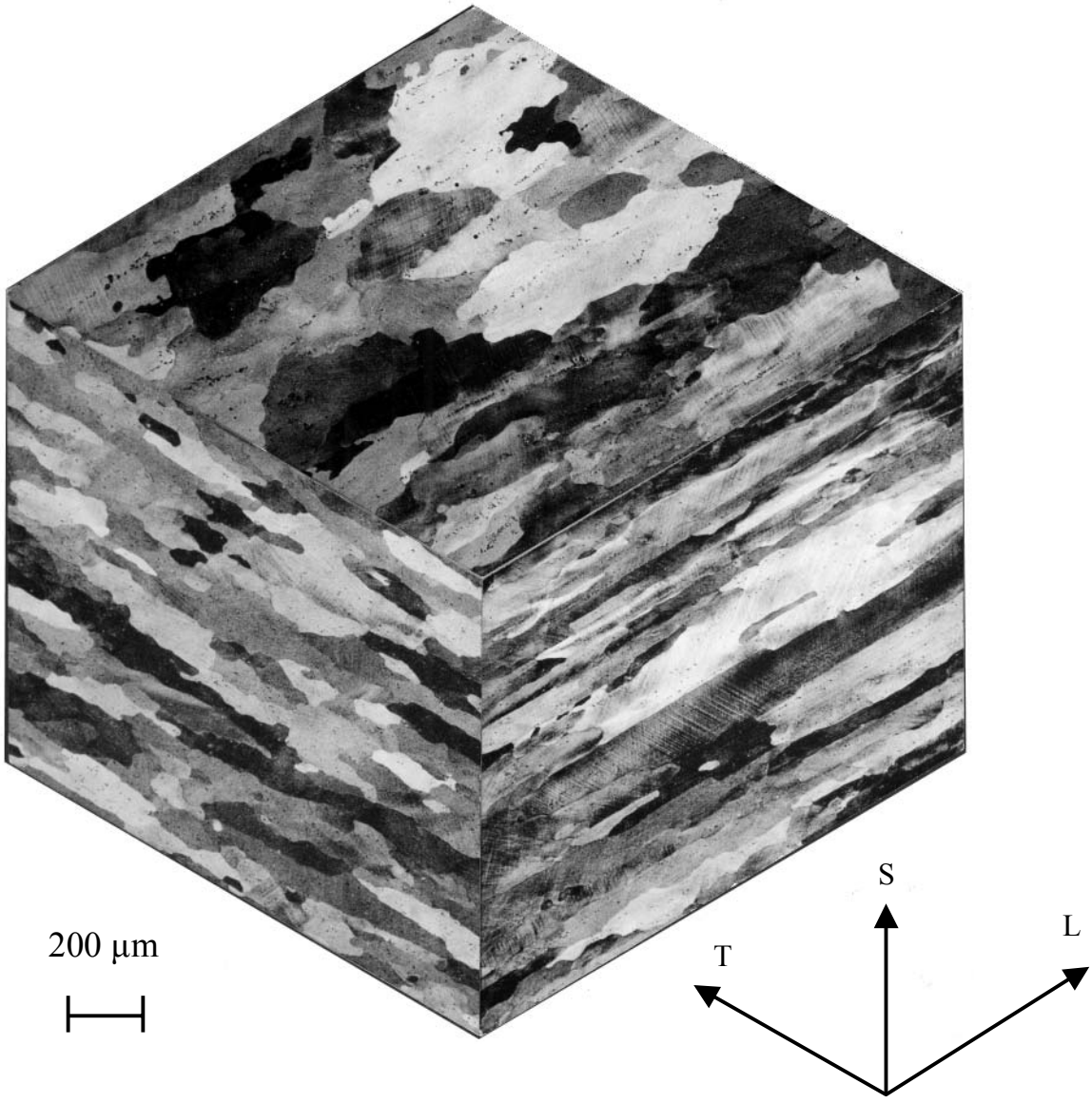

(a) Near-surface location.

Figure 7. Microstructure of RX226-T8 1.5-inch thick plate as a function of through-thickness plate location.

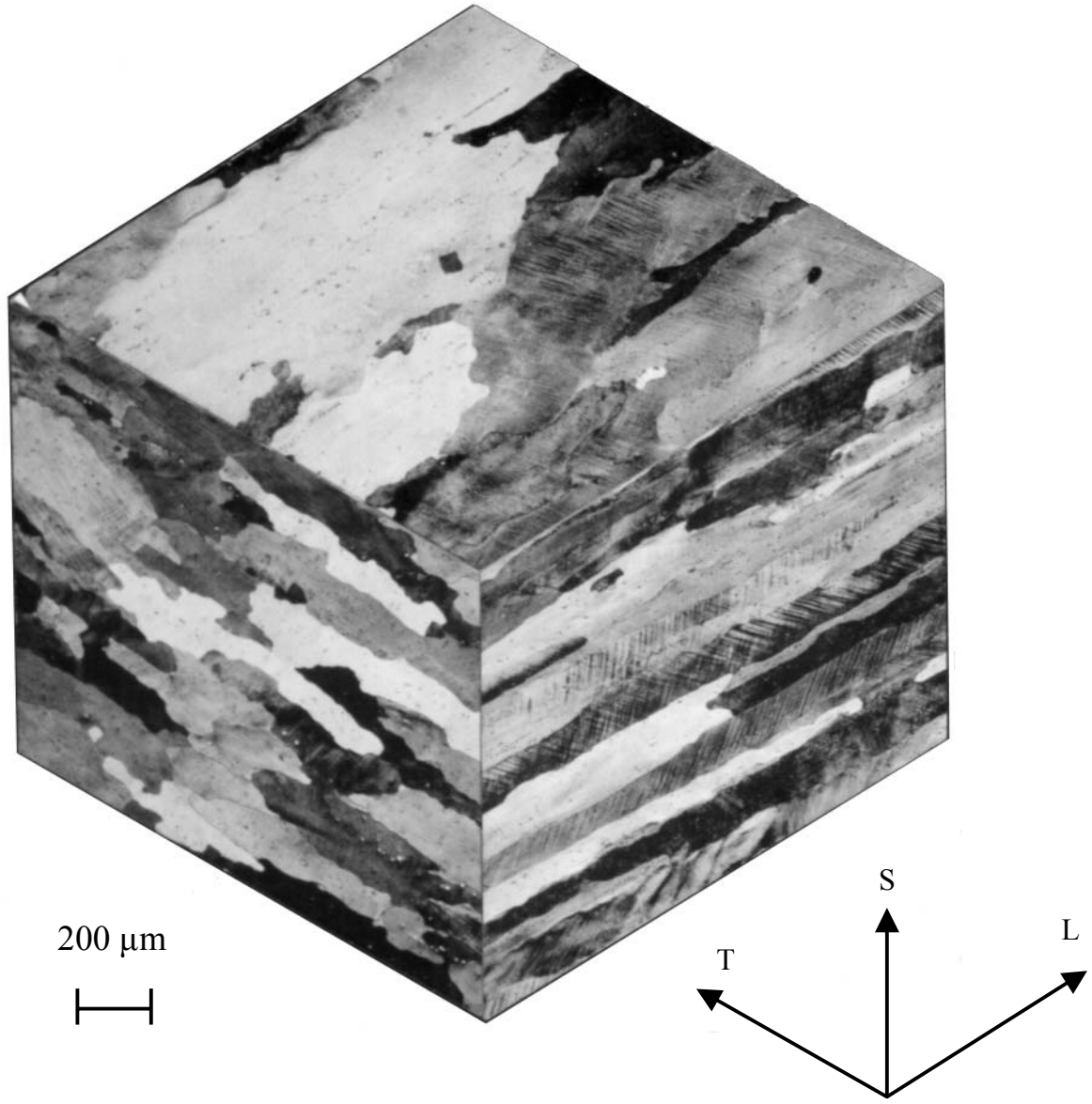

(b) Mid-plane location.

Figure 7. Concluded.

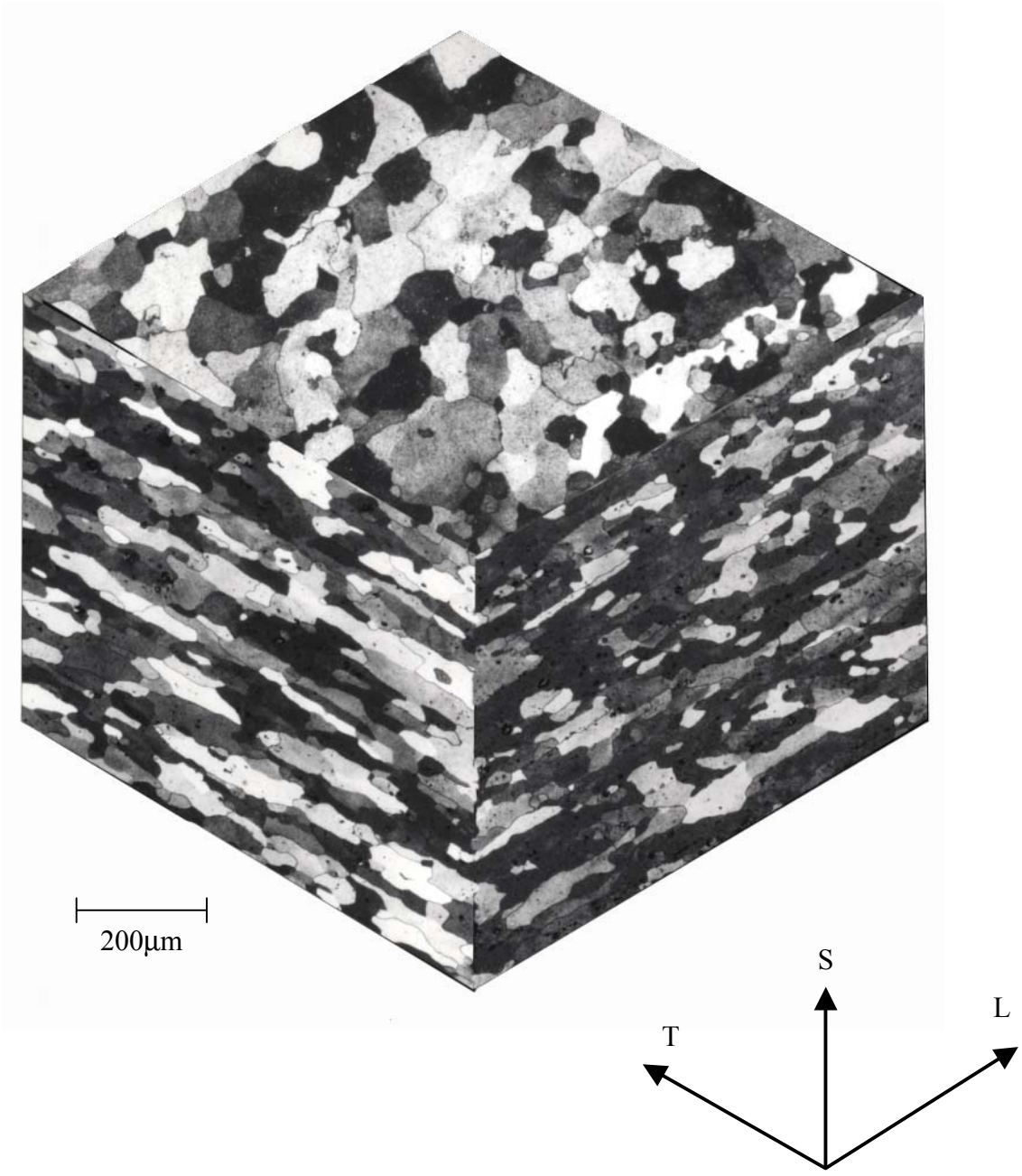

(a) C415-T8

Figure 8. Microstructure at the mid-plane of C415-T8 and C416-T8 0.090-inch thick sheets.

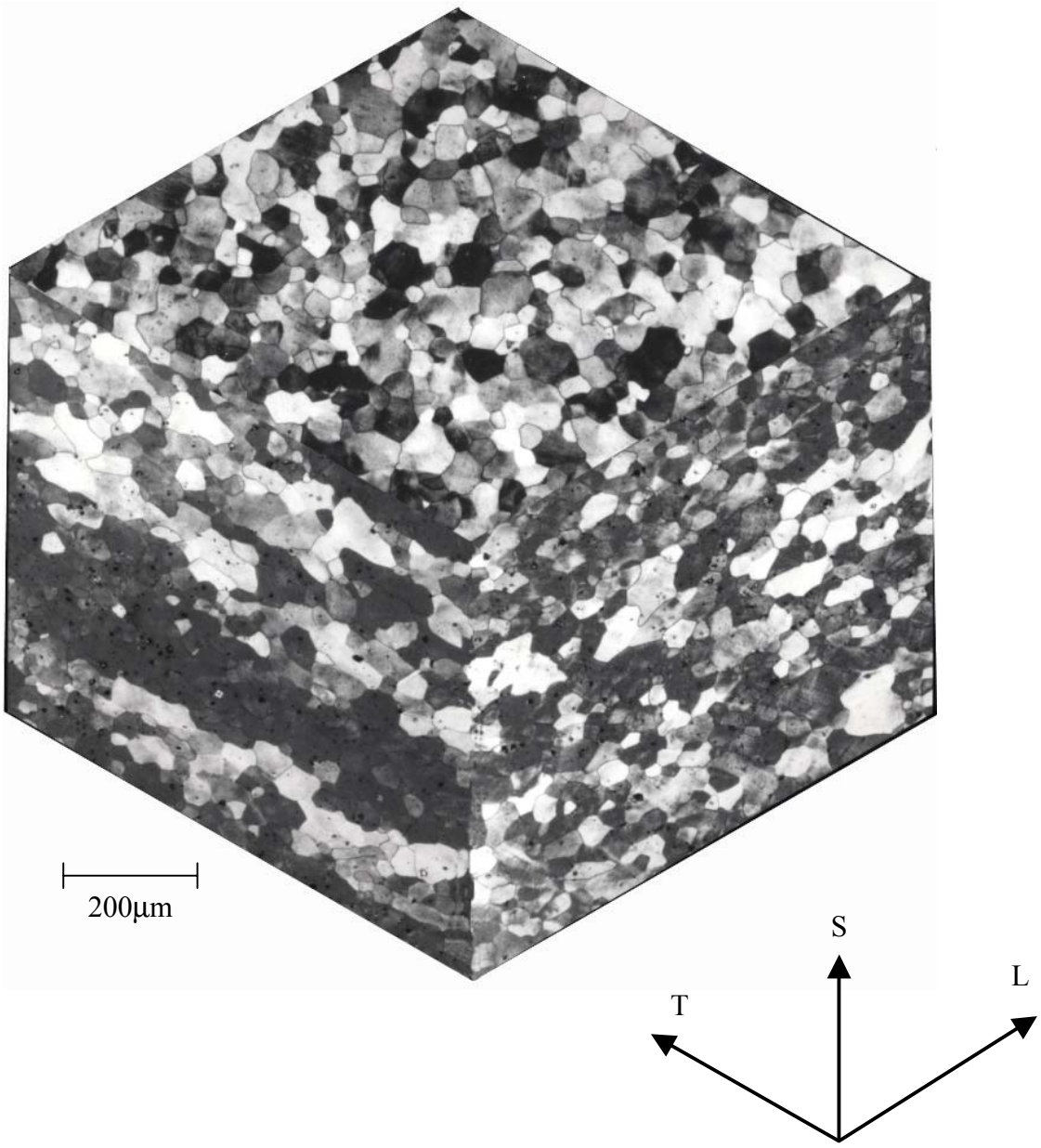

(b) C416-T8

Figure 8. Concluded.

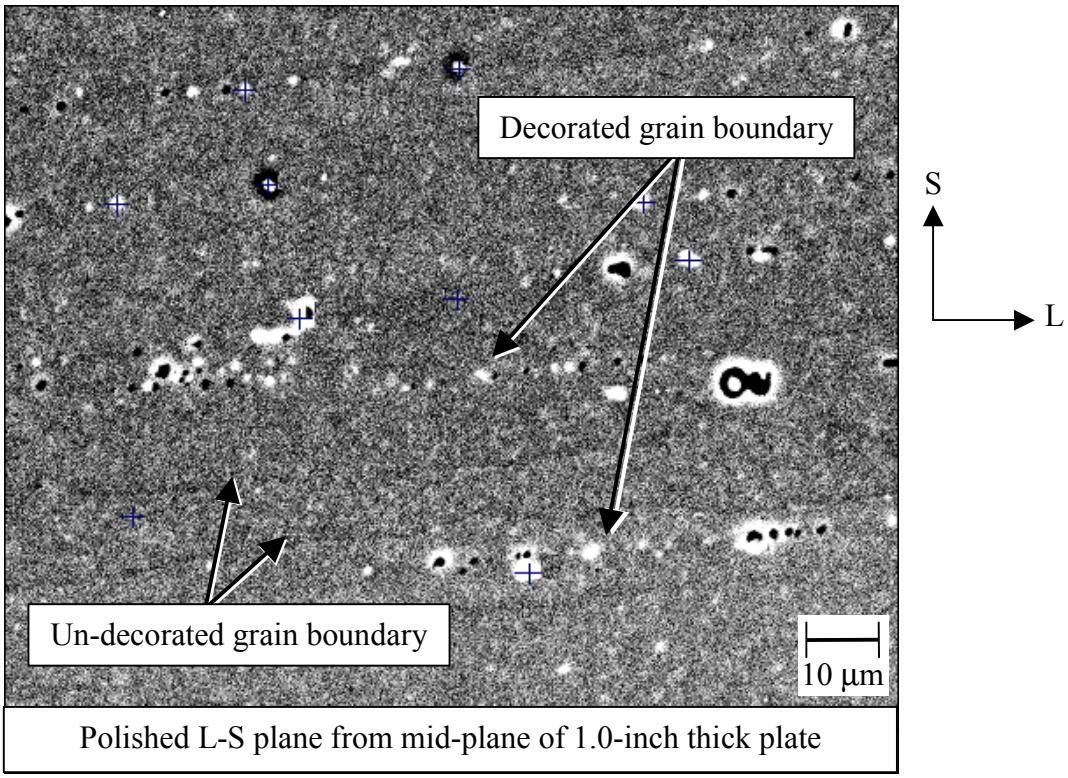

Figure 9. Backscattered SEM image illustrating typical second phase particle distribution observed in RX226-T8 plate.

Previously reported transmission electron microscope (TEM) studies of the C415 and C416 sheets revealed that the primary strengthening phases were Ω (AlCu) and θ' (Al_2Cu), with some S' (Al_2CuMg) present for C415 [2]. Analysis also identified incoherent second phase particles of Al_7Cu_2Fe, Al_5CuZr_2, and $Al_{20}Cu_2Mn_3$, 1-5 µm in diameter, aligned along grain boundaries [2].

In the Al-Cu-Mg-Ag alloy system, the Cu and Mg solute levels, often expressed as Cu/Mg ratio, and the solid solubility limit, determine the strengthening precipitates present [16, 17]. This relationship is illustrated graphically in Figure 10, which has been adapted from Cassada and Bartholomeusz [16] and which is based in part on the work of Polmear [17]. Depending upon the Cu and Mg solute levels and aging practice, the microstructure could contain: (1) Ω and θ', (2) Ω, θ', and S', or (3) S' precipitates [2, 16]. Cu and Mg solute levels for each of the RX226 plates and for C415 and C416, from Table 1, are plotted in Figure 10 and indicate that C416 should contain Ω and θ' precipitates and C415 should contain Ω, θ', and S' precipitates. While the Cu and Mg levels are lower in RX226 than both C415 and C416, which should result in improved thermal stability, the Cu/Mg ratio is similar to C416. Although the strengthening precipitates were not specifically evaluated in this study for RX226, the primary strengthening phases have been assumed to be Ω and θ', since the Cu and Mg solute levels, the Cu/Mg ratio and the aging conditions for RX226 are similar to C416.

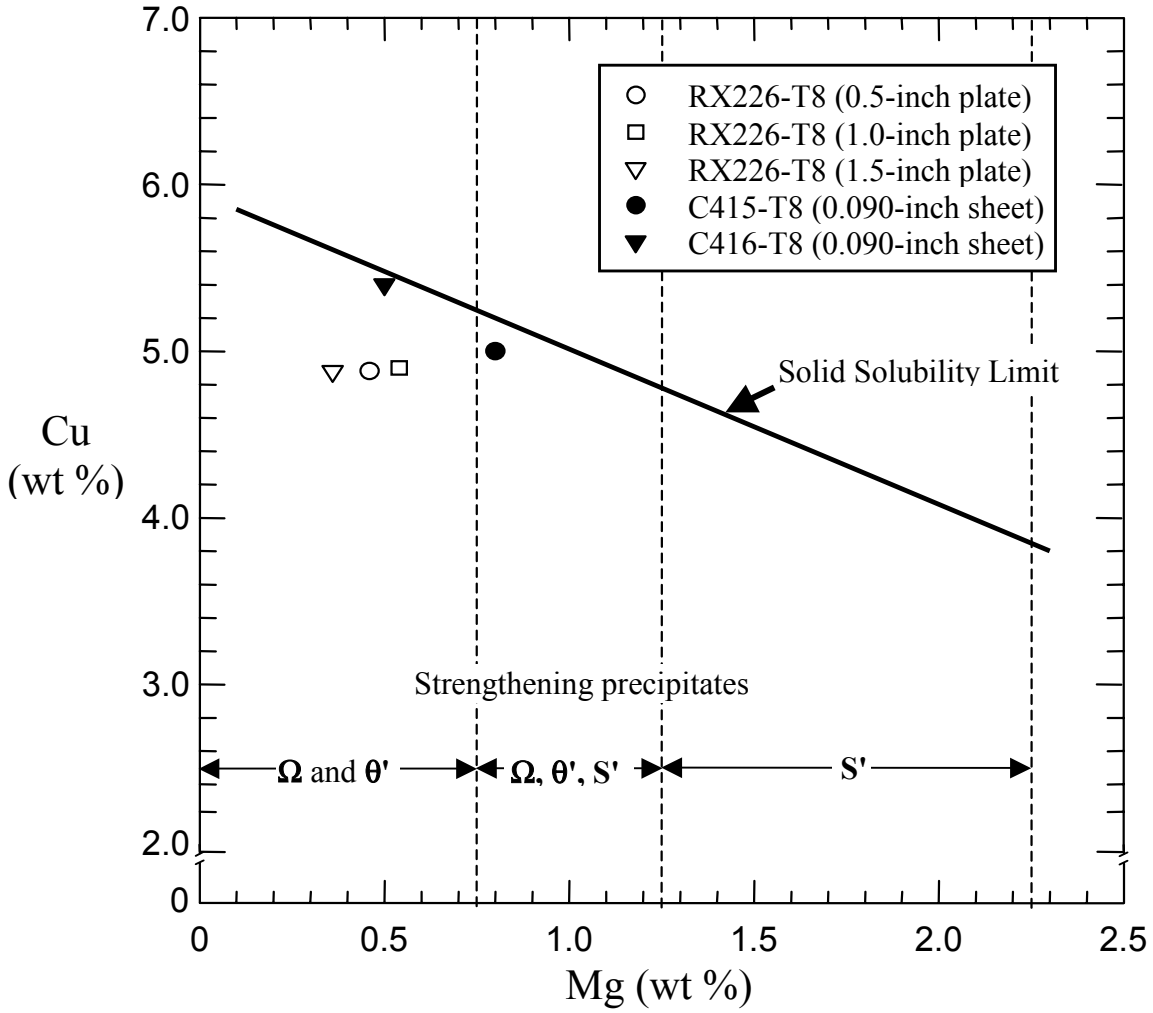

Figure 10. Effect of Cu and Mg solute levels on the phases present in Al-Cu-Ag-Mg alloys, based on the work of Cassada and Bartholomeusz [16] and Polmear [17].

Tensile Properties

Mechanical properties reported in this study are the results of testing the 1.0-inch thick plate. The 0.5-inch and 1.5-inch plates were reserved for later property testing. Table 2 and Figures 11-14 present ambient temperature tensile properties of the 1.0-inch thick RX226-T8 plate as a function of orientation and plate location. Table 2 provides individual specimen test results and average values. Figures 11-14 show the minimum, average and maximum test values for yield and ultimate tensile strengths, modulus and ductility.

For both plate locations and orientations, yield and ultimate tensile strengths varied by about 2%, indicating that the strength properties were relatively isotropic throughout the plate. While the variations observed were small, comparison of Figures 11 and 12 show that anisotropy was slightly greater for yield strength than for ultimate tensile strength. Figure 11 also shows that yield strength was lowest for the transverse orientation measured at the near-surface plate location, but agreed within 0.5% among the other orientation-plate location combinations.

Figure 12 shows that ultimate tensile strength was highest for the transverse orientation measured at the mid-plane, but varied by no more than 0.5% among the other orientation-plate location combinations. The isotropic strength behavior can be attributed to the recrystallized grain structure of the plate [16], and was not significantly affected by the elongated grain morphology.

As depicted in Figure 13, the modulus of the RX226-T8 plate also exhibited very little anisotropy, with average values for each orientation and plate location within 2% of the overall average value. Greater variations in ductility were observed with orientation and plate location, as shown in Figure 14. The degree of ductility anisotropy was similar for the mid-plane and near-surface plate locations, with elongation values approximately 16% lower for the transverse orientation. Ductility was lower at the mid-plane than near-surface location, with values 2% lower for the longitudinal orientation compared to 6% lower for the transverse orientation. The higher degree of anisotropy in elongation values compared to strength suggests a greater influence of the elongated grain morphology and distribution of grain boundary second phase particles. Second phase particles have been shown to be brittle and detrimental to ductility and fracture toughness in Al-Cu-Mg-Ag alloys [18-20].

Table 2. Tensile Properties of RX226-T8 Plate as a Function of Orientation and Through-thickness Plate Location.

Orientation	Plate Location 1.0-inch plate	Yield Strength, ksi	Ultimate Tensile Strength, ksi	Modulus, Msi	% Elongation, 1.0-inch Gage length
Longitudinal	Near-surface	68.7	73.6	10.6	10.2
		69.3	74.4	10.8	11.1
Average		68.9	74.0	10.7	10.7
Longitudinal	Mid-plane	69.7	74.8	10.7	10.5
		69.3	74.6	10.7	10.3
Average		69.5	74.7	10.7	10.4
Transverse	Near-surface	68.1	74.3	10.1	8.7
		68.1	74.7	10.8	9.6
Average		68.1	74.5	10.5	9.2
Transverse	Mid-plane	69.5	75.7	10.7	8.5
		69.6	75.8	10.8	8.7
Average		69.6	75.7	10.8	8.6

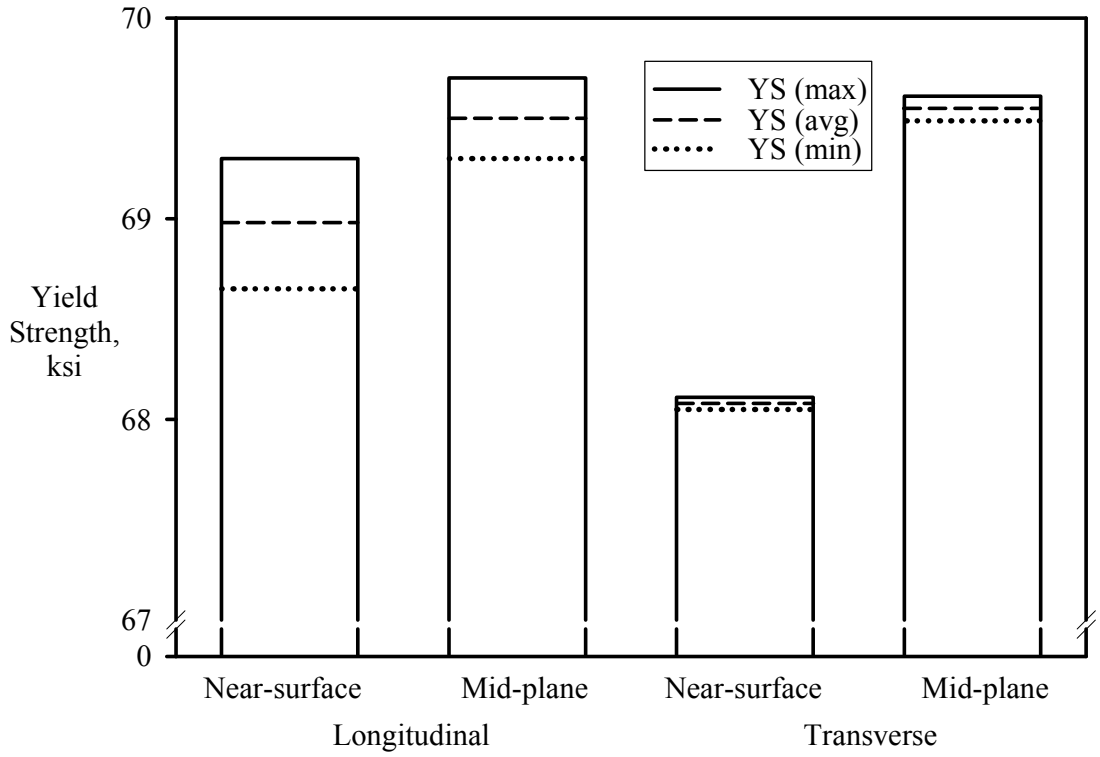

Figure 11. RX226-T8 yield strength as a function of orientation and plate location.

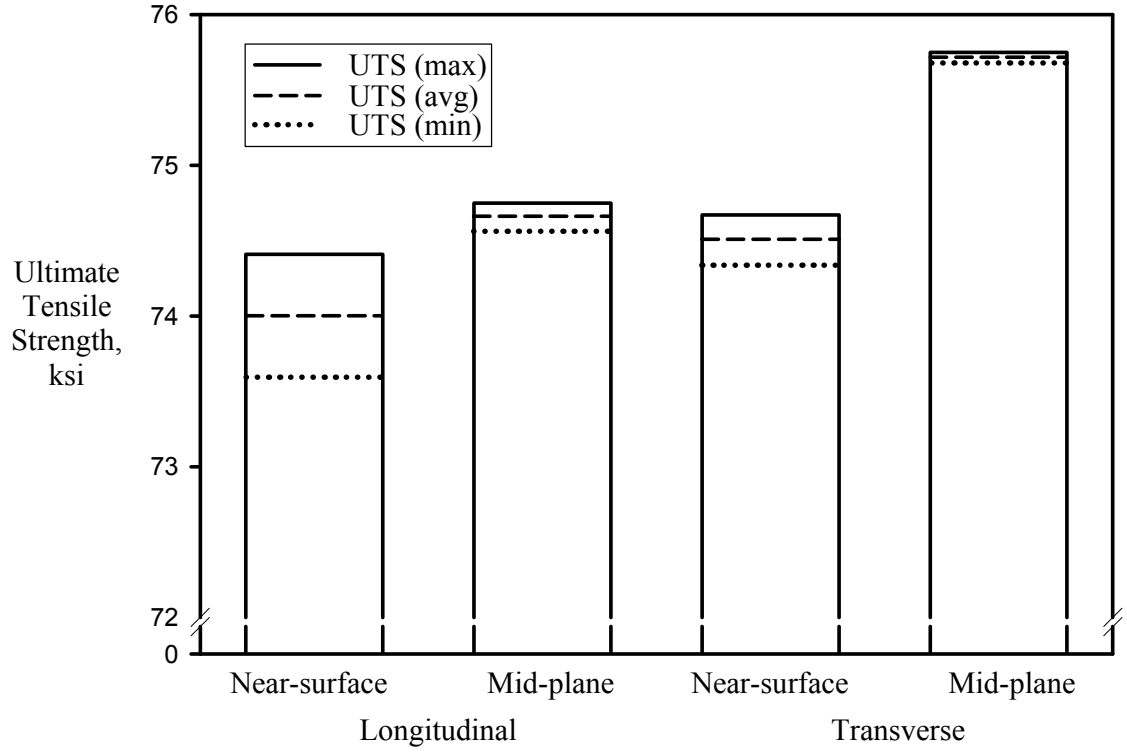

Figure 12. RX226-T8 ultimate tensile strength as a function of orientation and plate location.

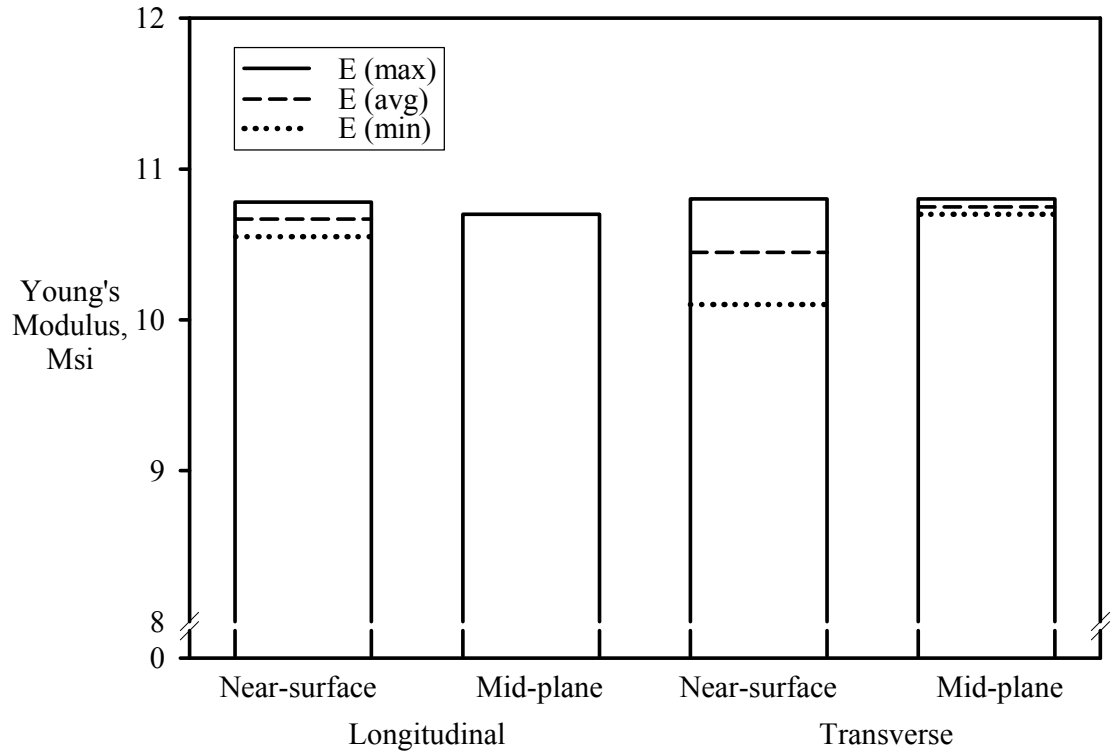

Figure 13. RX226-T8 modulus as a function of orientation and plate location.

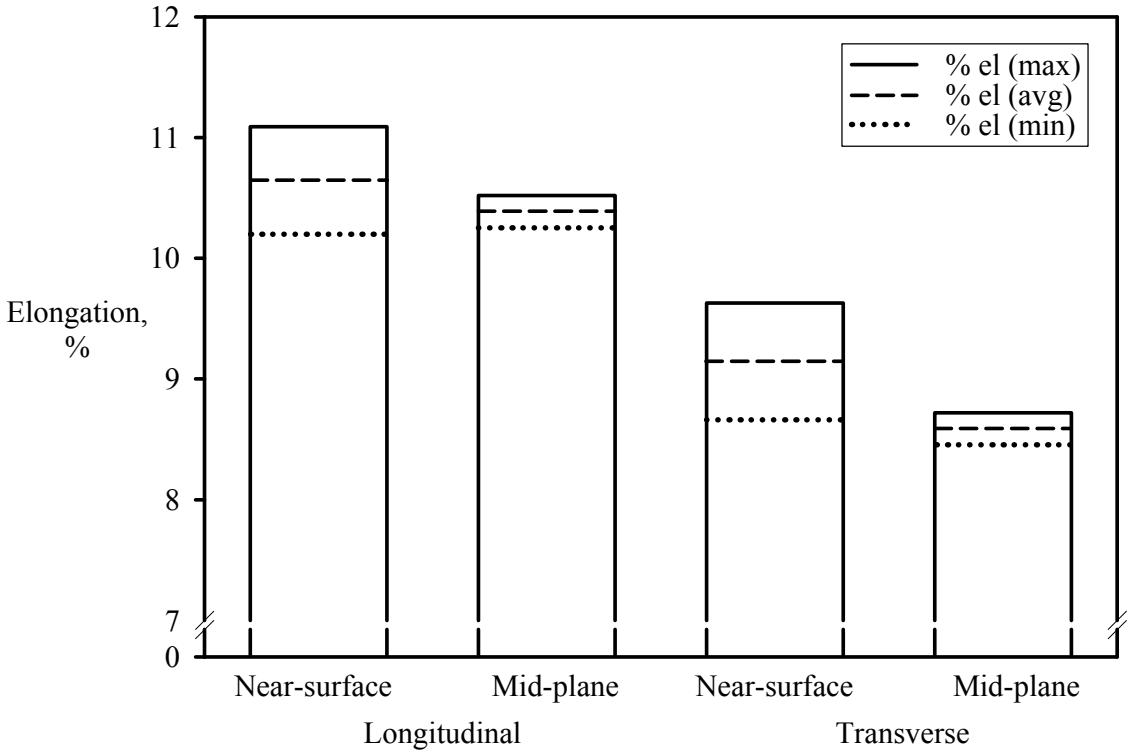

Figure 14. RX226-T8 ductility as a function of orientation and plate location.

Tensile properties of the 1.0-inch thick RX226-T8 plate are compared with data for C415-T8 and C416-T8 0.090-inch thick sheet [3] in Table 3. For all of the materials, the results represent mechanical properties based on tests with 0.090-inch thick specimens centered at the mid-plane of the product form. The yield and ultimate tensile strengths of the RX226 plate were within 5% of values for C415 and C416 for both orientations. The modulus of the RX226 plate was approximately 4% higher for both orientations when compared to C415 and C416 sheet. The variation in yield strength, ultimate tensile strength and modulus with orientation was less than 4% for C415 and C416 sheet and less than 2% for RX226, indicating that these properties were essentially isotropic for both product forms. The ductility of the RX226 plate was intermediate to that of C415 and C416 sheet with higher longitudinal ductility for C416 and higher transverse ductility for C415. The anisotropy observed in the ductility of RX226 plate exceeded that for C415 sheet but was less than that for C416 sheet. Overall, the tensile property results indicated that sheet gage material machined from the RX226 plate exhibited tensile properties comparable to rolled C415 and C416 sheet. While the degree of cold work was higher in the rolled sheet than the plate and might be expected to result in higher sheet tensile strengths, the similarity in tensile properties may be attributed to the recrystallized grain structure in both product forms.

Table 3. Mid-Plane Tensile Properties of RX226-T8 Plate Compared to C415-T8 and C416-T8 Sheet.

Orientation	Alloy/ Product Form	Yield Strength, ksi	Ultimate Tensile Strength, ksi	Modulus, Msi	% Elongation, 1.0-inch Gage length
Longitudinal	RX226-T8 1.0-inch plate	69.5	74.7	10.7	10.4
Transverse		69.6	75.7	10.8	8.6
Longitudinal	C415-T8 0.090-inch sheet [3]	73.3	78.6	10.3	9.0
Transverse		70.8	77.2	10.3	10.5
Longitudinal	C416-T8 0.090-inch sheet [3]	72.1	76.1	10.3	10.9
Transverse		69.6	74.4	10.2	8.5

Fracture Toughness Properties

Fracture toughness was determined using C(T) specimens of 0.090-inch thickness machined from the near-surface and mid-plane locations of the 1.0-inch thick RX226-T8 plate. The results of the individual crack growth resistance curves (R-curves) are shown in Figures 15-18 as a function of orientation and thickness location. Figures 15 and 16 illustrate the effect of orientation on R-curve behavior at the mid-plane and near-surface locations, respectively. The R-curves are re-plotted in Figures 17 and 18 to illustrate the variation with thickness location for L-T and T-L orientations, respectively. Initiation fracture toughness (K_{JIci}) and tearing modulus (T_R) values are provided in Table 4 and illustrated graphically in Figures 19 and 20. Figures 19 and 20 show the minimum, average, and maximum values to illustrate the range of K_{JIci} and T_R as a function of orientation and thickness location. The initial ligament and the thickness of these compact specimens met the plain strain validity requirements in Equation 2; thus, the K_{JIci} values were valid per ASTM E1820-01 [7].

Figure 15 illustrates that for the mid-plane location, the R-curves for replicate L-T and T-L specimens were fairly systematically grouped, with somewhat greater scatter observed for the T-L orientation. The L-T orientation exhibits higher toughness, as evidenced by the overall higher R-curves and indicated by higher K_{JIci} and T_R values calculated from the R-curves. The values provided in Table 4 indicate that K_{JIci} was more than 20% higher and T_R was nearly 40% higher for the L-T orientation. The bar graphs in Figures 19 and 20 illustrate that, for the mid-plane location, the range of K_{JIci} values was greater for the T-L orientation while the range of T_R values was greater for the L-T orientation.

For the near-surface plate location (Figure 16), the R-curves for replicate L-T and T-L specimens were less systematically grouped than was observed for the mid-plane location. While the average initiation fracture toughness (Table 4) was approximately 10% higher for the T-L orientation, Figure 19 shows that the range of K_{JIci} for the T-L orientation nearly encompasses the L-T data range, suggesting relatively isotropic initiation toughness at the near-surface plate location. Tearing modulus values were approximately 30% higher for the L-T orientation, with the range of T_R values similar for both orientations (Figure 20).

Figure 17 illustrates that for the L-T orientation, the R-curves for specimens from the mid-plane were generally higher and exhibited less scatter than for those specimens machined from the near-surface location of the plate. The average initiation toughness and tearing modulus for the mid-plane were more than 20% higher than the corresponding values for the near-surface location (Table 4). The range of K_{JIci} and T_R values were similar for each plate location and were greater for the T_R values (Figures 19 and 20).

For the T-L orientation, shown in Figure 18, the shape and scatter of the overall R-curves were similar for both orientations. The average K_{JIci} values (Table 4) were within 5% for the near-surface and mid-plane locations. Figure 19 illustrates that the range of the K_{JIci} data was similar for both plate locations. The average T_R was approximately 20% greater for material from the mid-plane (Table 4), with the range of values greater for the near-surface location (Figure 20).

The variability observed in K_{JIci} and T_R values may be associated with the offset definition of initiation toughness [21] along with the difficulty in measuring steeply rising R-curves for small changes in crack length [22].

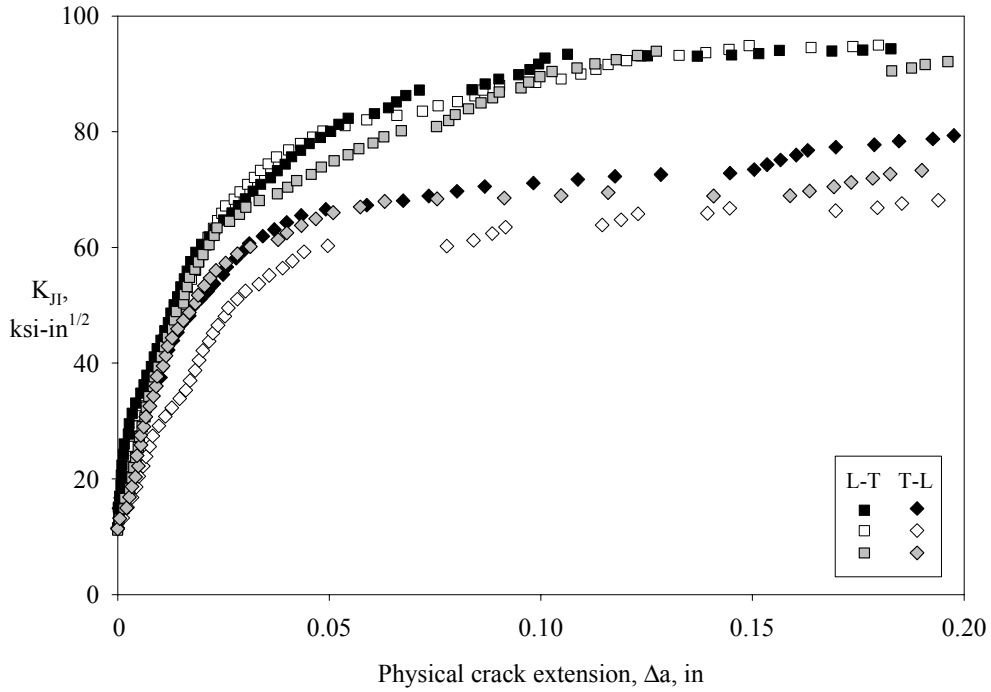

Figure 15. Variation in R-curve behavior with specimen orientation for the mid-plane location in 1.0-inch thick RX226-T8 plate.

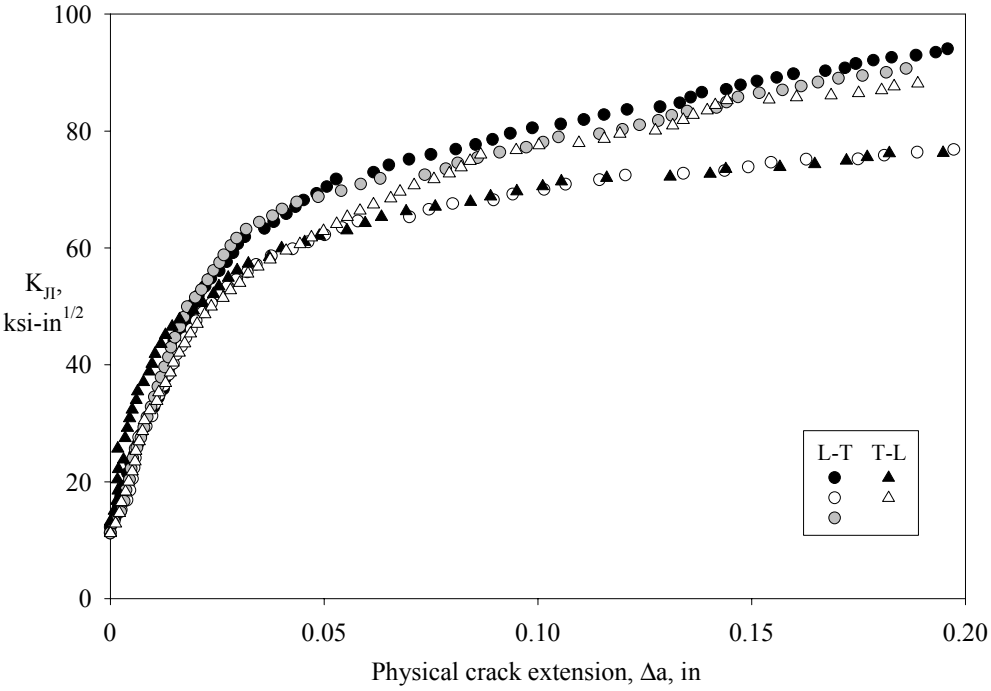

Figure 16. Variation in R-curve behavior with specimen orientation for the near-surface location in 1.0-inch thick RX226-T8 plate.

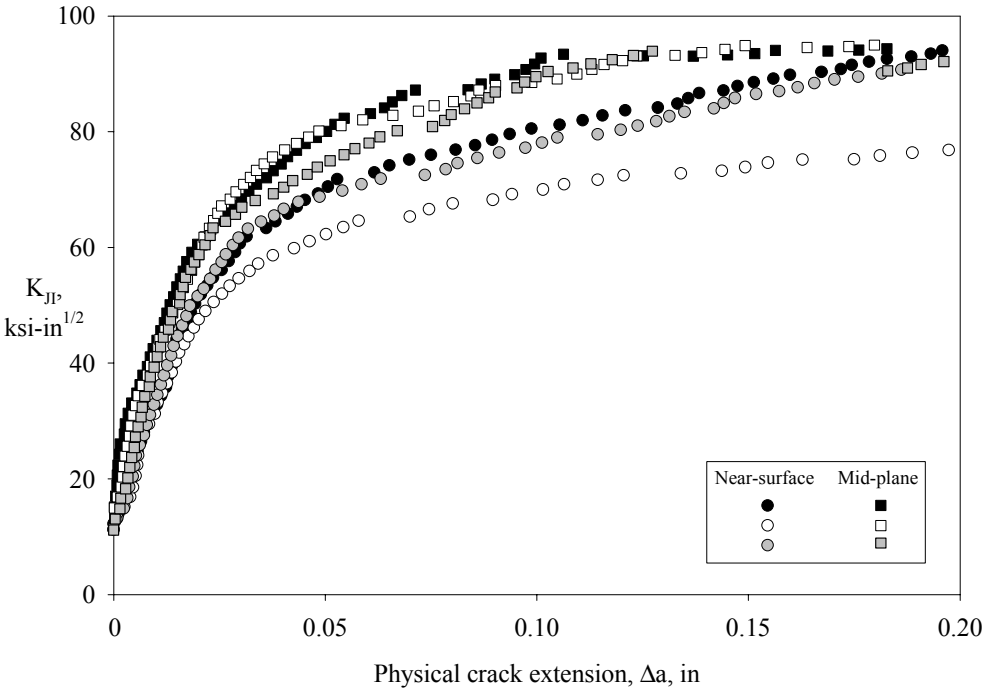

Figure 17. Variation in R-curve behavior for the L-T orientation with through-thickness location in 1.0-inch thick RX226-T8 plate.

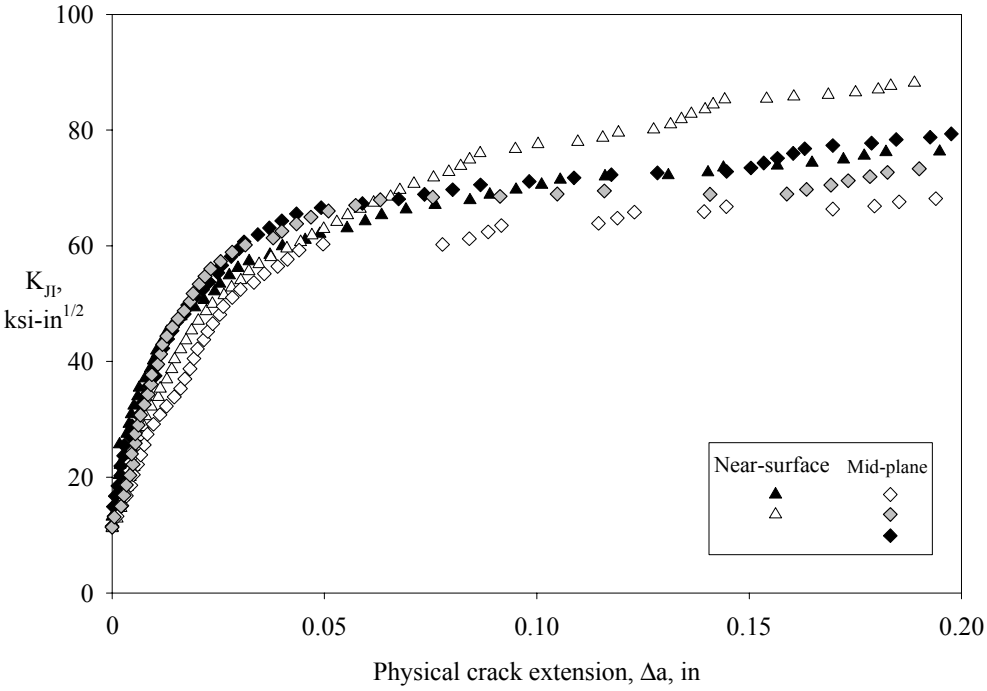

Figure 18. Variation in R-curve behavior for the T-L orientation with through-thickness location in 1.0-inch thick RX226-T8 plate.

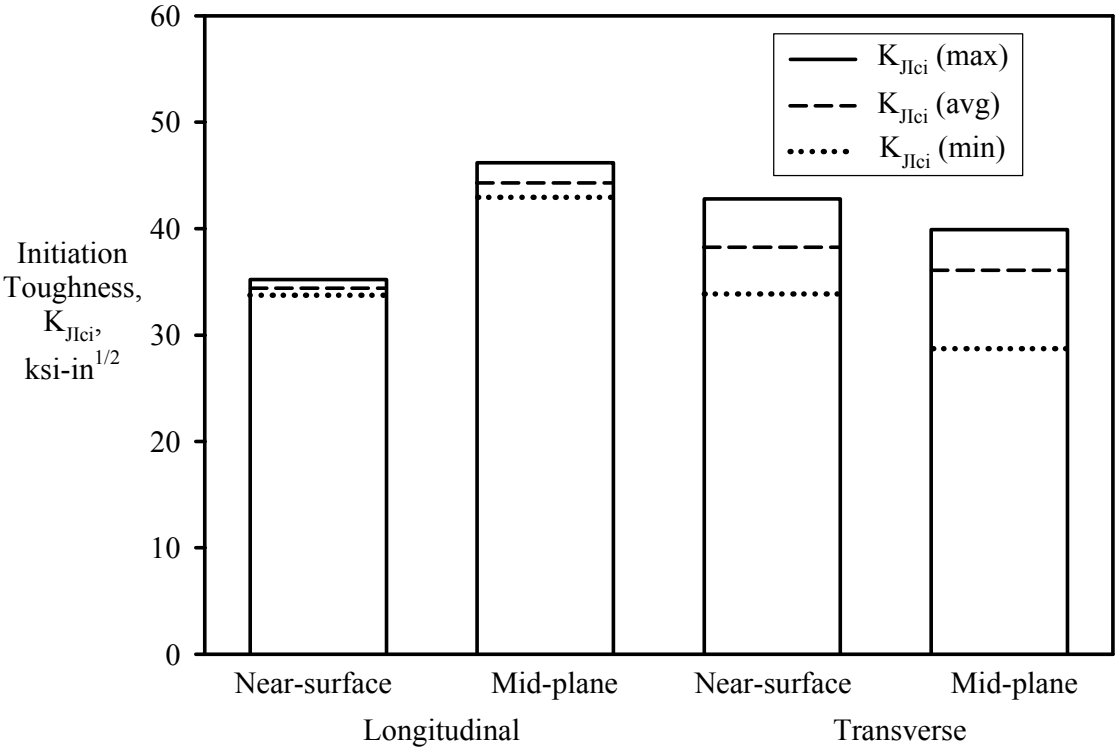

Figure 19. RX226-T8 initiation toughness, K_{JIci}, as a function of orientation and plate location.

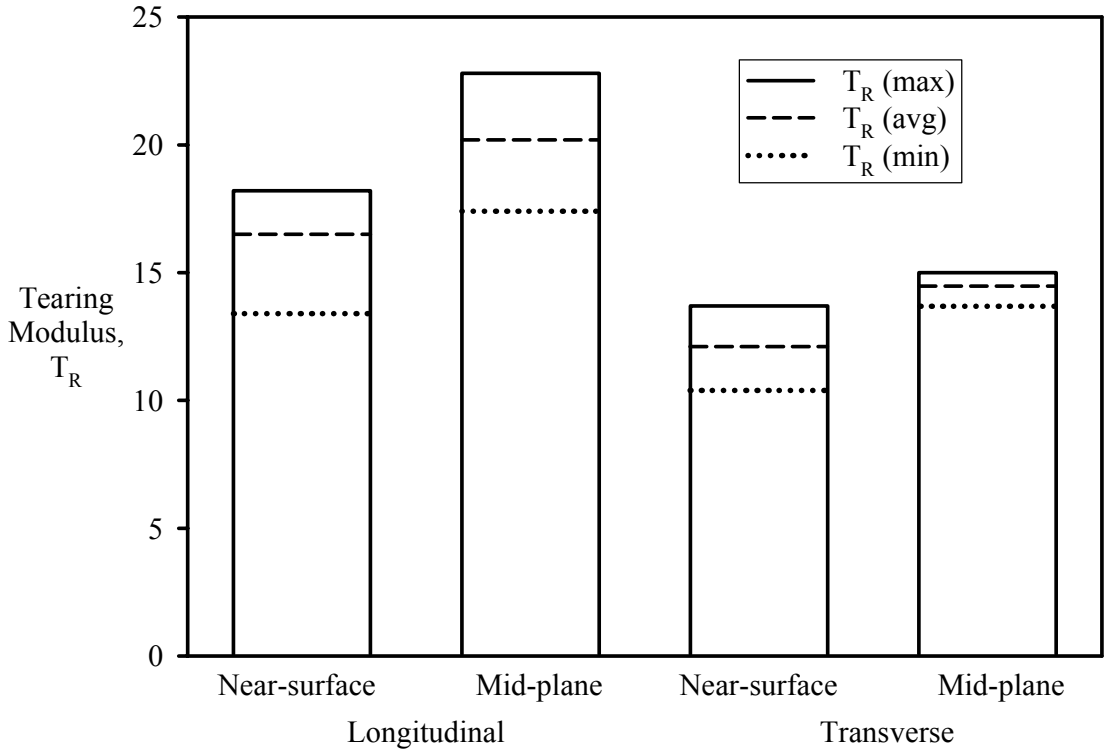

Figure 20. RX226-T8 tearing modulus, T_R, as a function of orientation and plate location.

Table 4. RX226-T8 Fracture Toughness Properties as a Function of Orientation and Through-thickness Plate Location.

Orientation	Plate Location	K_{JIci}, ksi-in$^{1/2}$	T_R	Crack Growth Plane	Fracture Profile
L-T	Near-surface	34.1	18.2	In-plane	Slant
		33.8	13.4	In-plane	Slant
		35.2	17.8	In-plane	Slant
Average		34.4	16.5		
L-T	Mid-plane	46.2	20.5	In-plane	Slant
		43.9	22.8	In-plane	Slant
		42.9	17.4	In-plane	V-shear
Average		44.3	20.2		
T-L	Near-surface	42.8	10.4	In-plane	Slant
		33.9	13.7	In-plane	V-shear
Average		38.3	12.1		
T-L	Mid-plane	39.9	14.7	In-plane	Slant
		28.7	15.0	In-plane	Slant
		39.7	13.7	In-plane	Slant
Average		36.1	14.5		

Fracture toughness measured at the mid-plane of the RX226-T8 plate evaluated during this study is compared in Table 5 with results from prior studies [2] of C415-T8 and C416-T8 sheet. The results for C415 and C416 sheet represent the average of duplicate specimens, with specimen geometry, data collection, and analysis the same as reported for the RX226 plate. The initiation toughness levels for RX226 plate were as much as 16% (L-T) to 37% (T-L) lower than for the sheet products. The resistance to stable crack growth, indicated by tearing modulus in Table 5, was considerably higher in the L-T orientation for the plate compared to the sheet product form, and values were comparable in the T-L orientation. Anisotropy in initiation toughness for RX226 was more than 20%, which was higher than observed for C415 (4%) but comparable to C416 (16%). Tearing modulus anisotropy for RX226 was very large (39%), which was considerably higher than for either C415 (23%) or C416 (5%).

Table 5. Yield Strength and Fracture Toughness of RX226-T8 Plate Compared to C415-T8 and C416-T8 Sheet.

Orientation	Alloy/ Product Form	K_{JIci}, ksi-in$^{1/2}$	Tearing Modulus, T_R	YS	YS / K_{JIci}
L-T	RX226-T8 1.0-inch plate	44.3	20.2	69.5	1.57
T-L		36.1	14.5	69.6	1.93
L-T	C415-T8 0.090-inch sheet [2]	53.3	11.7	73.3	1.38
T-L		51.3	14.4	70.8	1.38
L-T	C416-T8 0.090-inch sheet [2]	49.4	12.3	72.1	1.46
T-L		57.5	12.9	69.6	1.21

The strength-toughness combination of the RX226-T8 plate, as shown in Figure 21, was lower than that of the C415 and C416 sheet for both orientations. The results shown illustrate that while the yield strength of RX226 was within 5% of that of the sheet products, initiation fracture toughness was considerably lower, particularly for the T-L orientation. The average yield strength to fracture toughness ratio (σ_{YS}/K_{JIci}) of the plate was 1.75 compared to approximately 1.4 for the sheet alloys. The RX226 plate evaluated in this study was laboratory produced material and is not fully representative of commercially produced plate. Refinements in the chemistry, aging, or thermomechanical processing of the plate are anticipated to result in improved properties. For example, Beffort, et al. [4] observed improvements in yield strength and fracture toughness of an Al-Cu-Mg-Ag alloy by using various two-step-aging procedures and optimized thermomechanical processing. Specifically, yield strength was improved due to increased density of strengthening precipitates. The fracture toughness was observed to increase when the size of the strengthening precipitates was decreased while equal volume fractions of Ω and θ' were maintained [4].

Figure 22 presents the variation in yield strength and fracture toughness with Cu/Mg solute ratio. The Cu/Mg ratio of the 1.0-inch thick RX226-T8 plate falls almost midway between the ratios of the C415 and C416 sheets. For the sheet materials, there is little effect on yield strength or toughness with changes in Cu/Mg ratio from 6 to 11. However, for the RX226-T8 plate at the intermediate Cu/Mg ratio of 9, there is a decrease of 10-30% in toughness compared with the sheet alloys, although yield strength remains within 5%. The decrease may reflect the experimental nature of the RX226 plate as compared with commercially produced sheet. However, the drop may also be related to the total solute content rather than to the Cu/Mg ratio. The total solute content of the 1.0-inch thick plate was about 5% less that that for C415 and C416. RX226 was designed for enhanced thermal stability and may not be the optimum chemistry for ambient temperature properties. It is anticipated that improvement in both strength and toughness could be achieved by increasing Cu and Mg solute levels to the solid solubility limit while optimizing processing to increase the density but control the size of strengthening precipitates, while still avoiding excessive second phase particles.

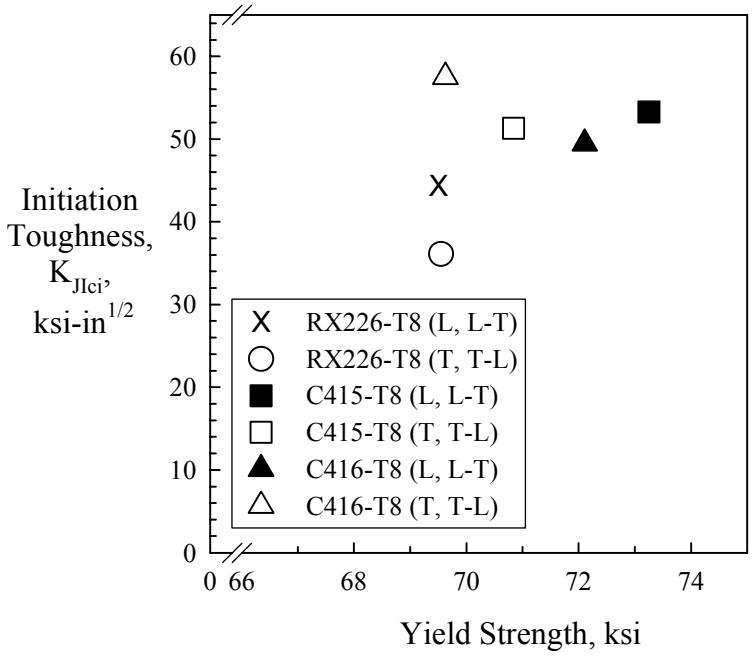

Figure 21. Al-Cu-Ag-Mg alloys strength/toughness behavior as a function of orientation at the mid-plane of the plate and sheet.

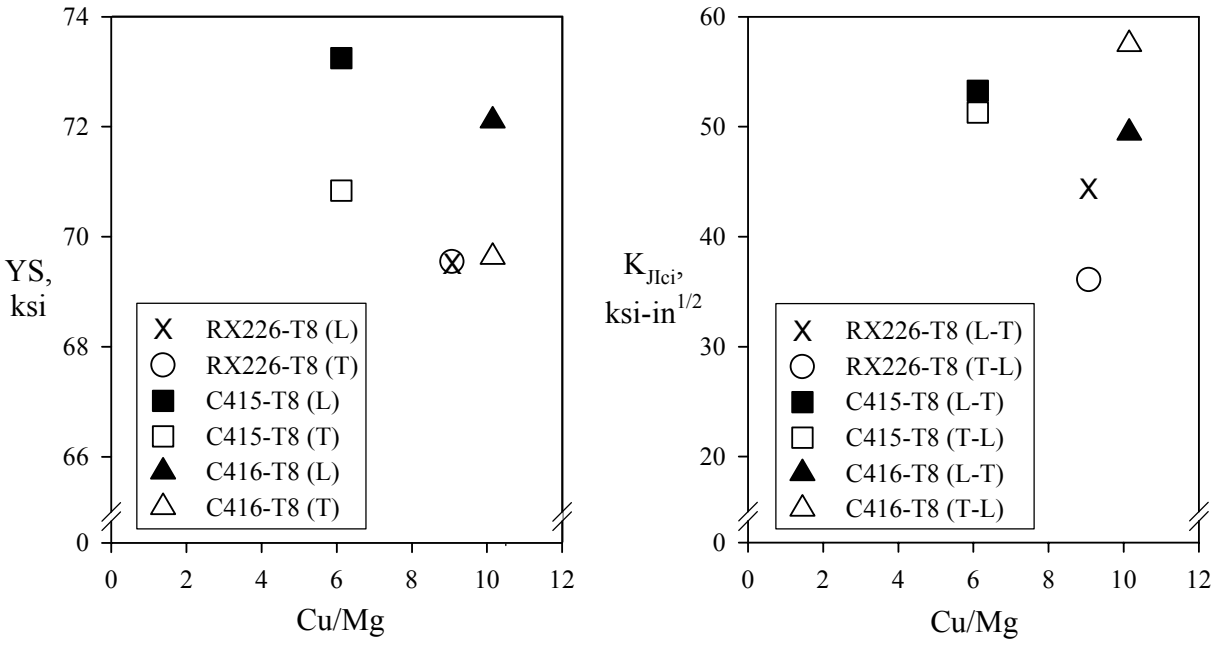

(a) Yield strength, YS (b) Initiation fracture toughness, K_{Jici}

Figure 22. Yield strength (YS) and initiation toughness (K_{JIci}) behavior of Al-Cu-Ag-Mg alloys as a function of Cu/Mg solute ratio and orientation at the mid-plane of the plate and sheet.

Fractography

The fracture surfaces of select compact tension fracture toughness specimens were examined macroscopically to evaluate the overall fracture morphology and microscopically to assess the fracture mode. Figure 23 defines the terminology used to describe the macroscopic fracture profiles and crack growth planes of the fracture specimens. As summarized in Table 4, with the exception of two specimens, all of the fractures examined developed slant fracture profiles. All specimens exhibited in-plane crack growth regardless of the fracture profile. Consequently, no attempt was made to correlate macroscopic fracture morphology with either K_{JIci} or T_R data in Table 4.

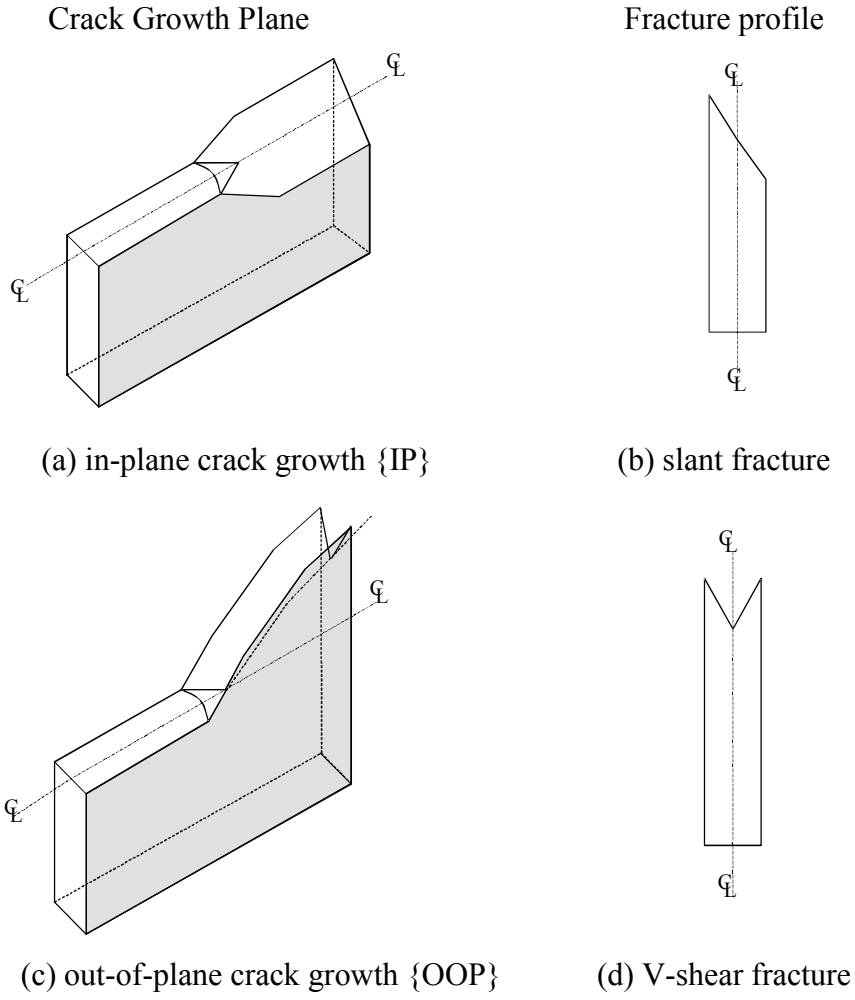

Figure 23. Schematic of compact tension specimen fracture morphology.

Microscopic examination was conducted in the SEM at two locations along the centerline of each specimen, in the plane strain region approximately 0.005 inches ahead of the pre-crack and in the plane stress region approximately 0.15 inches from the end of the pre-crack. A schematic identifying the regions of fracture examined is shown in Figure 24. Select fractographs are shown in Figures 25-29 to illustrate the trends in fracture features observed as a

function of orientation and plate thickness location. The direction of crack growth is to the right in each fractograph presented.

Fracture surfaces were generally characterized by a flat wedge-shaped region of plane strain fracture that initiated from the fatigue pre-crack and was bounded by slanted regions of plane stress fracture. The plane stress fracture regions extended to the specimen surfaces and grew larger with increasing crack growth until a transition to fully plane stress fracture occurred. The plane strain wedge was well defined in near-surface L-T orientation specimens, as shown in Figure 25(a). The plane strain wedge was less well defined in specimens that exhibited two types of linear fracture features at the onset of crack extension, as shown in Figures 25(b) and 26(b) for T-L orientation specimens from the near-surface and mid-plane locations, respectively.

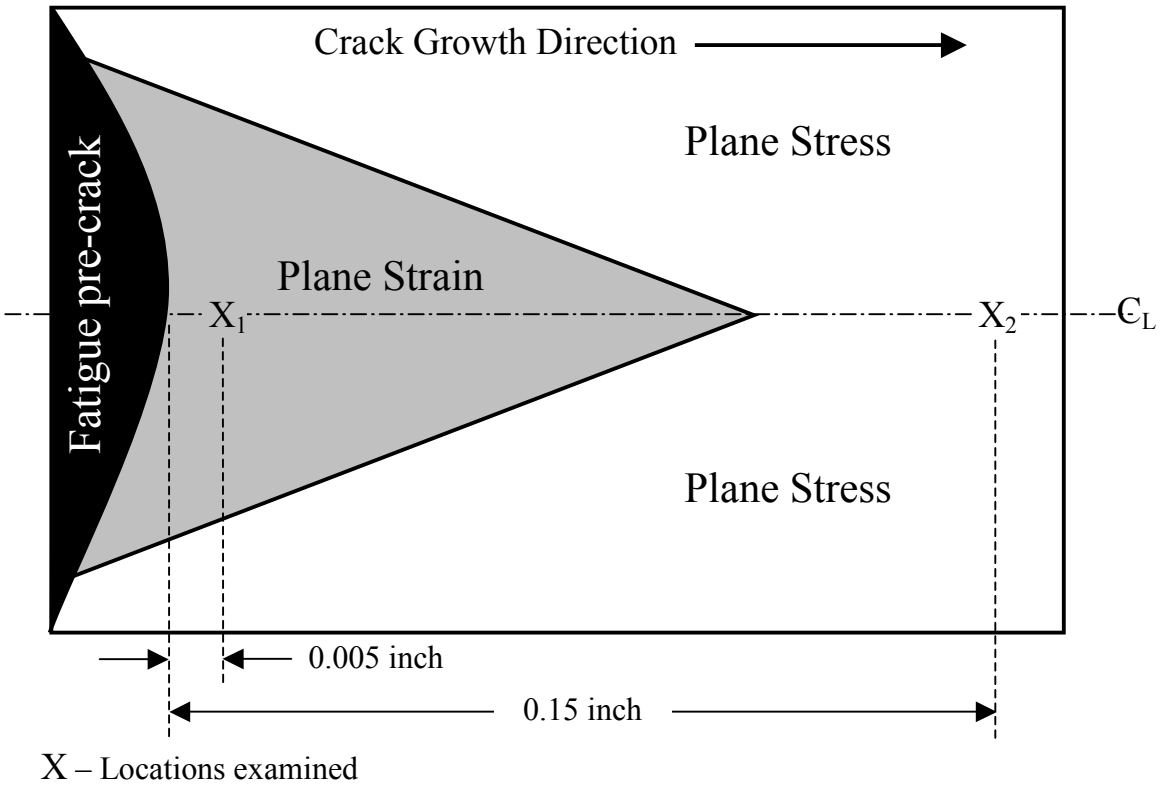

Figure 24. Schematic illustration of fracture regions.

Examination at higher magnification indicated that some of the linear features were primarily associated with microvoid coalescence at second phase particles aligned along grain boundaries, as shown by the examples in Figure 27. For this study, these features were termed regions of linear void coalescence (LVC). The elongated pancake-shaped grain morphology observed for the plate combined with the tendency for grain boundary particle decoration may have promoted the occurrence of long linear arrays of closely spaced second phase particles on some grain boundaries. The regions of LVC observed reflect fracture along these heavily decorated grain boundaries. In some cases, the length of LVC features were on the order of the length of the plane strain wedge (Figure 26(b)).

Other linear features were related to coarse, separated grain facets, as shown by the examples in Figure 28, and are referred to as intergranular cracks (IGC). Examination at higher magnification revealed dimples on the intergranular facets, as shown in Figure 28(b),

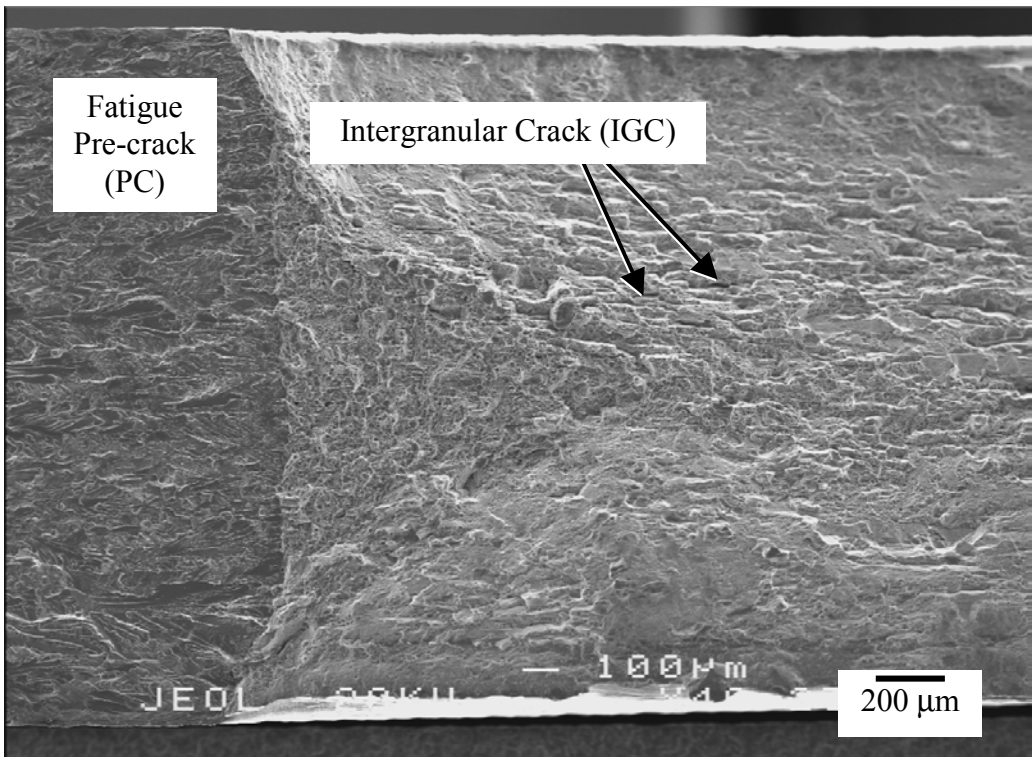

(a) L-T orientation.

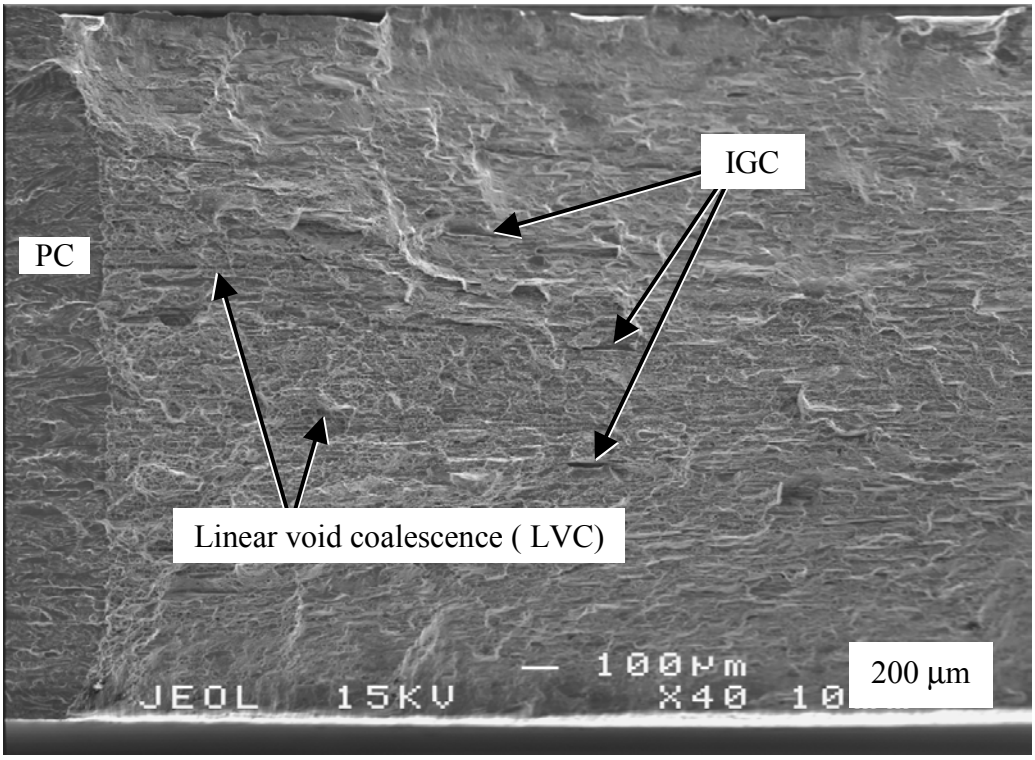

(b) T-L orientation.

Figure 25. Fractographs of RX226-T8 specimens machined at the near-surface location.

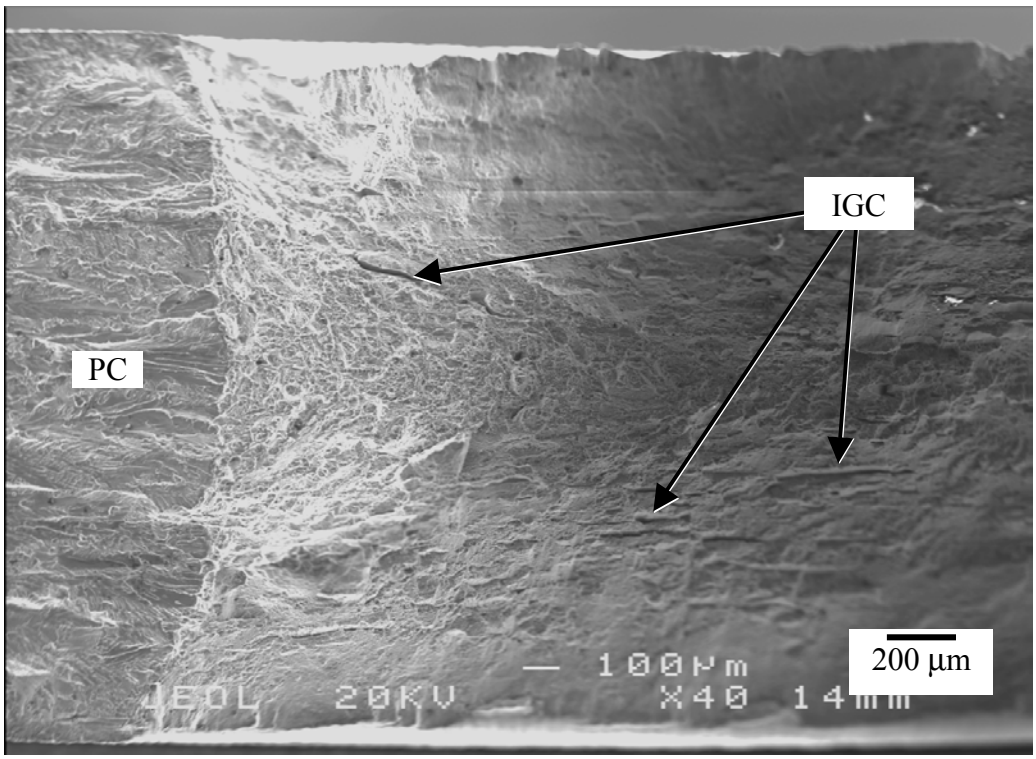

(a) L-T orientation.

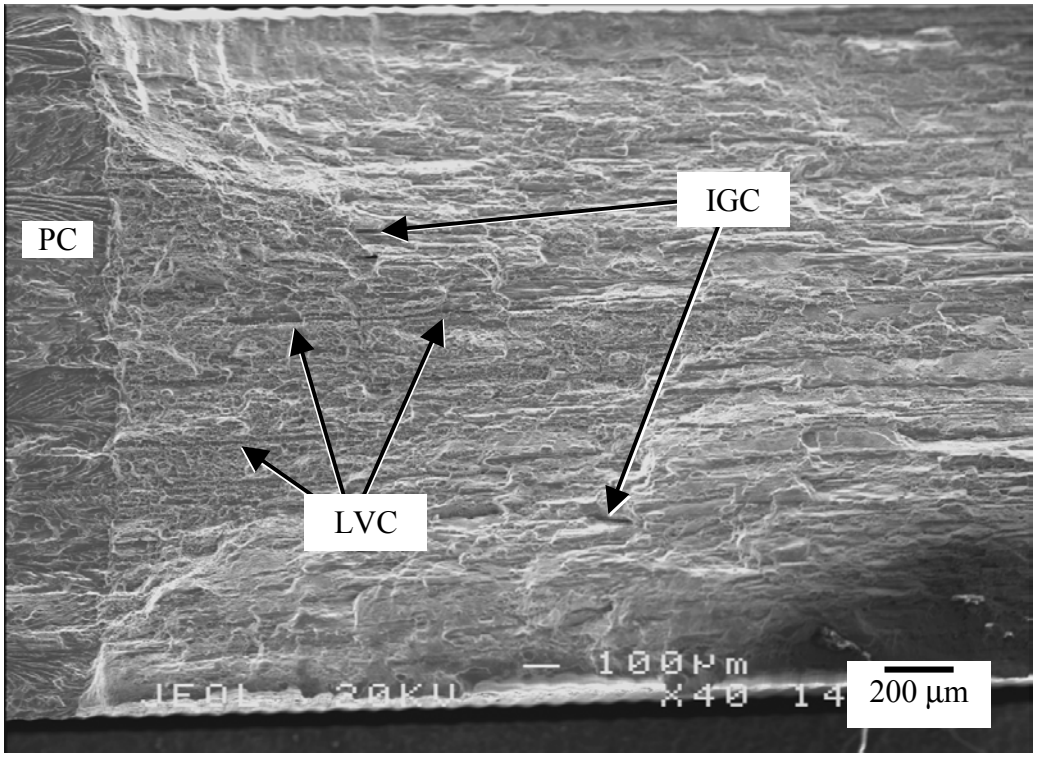

(b) T-L orientation.

Figure 26. Fractographs of RX226-T8 specimens machined at the mid-plane location.

suggesting that the fracture mode at these locations was by ductile intergranular fracture [23]. Both IGC and LVC, oriented predominantly parallel to the crack growth direction, were also observed in the region of plane stress crack growth on all fracture surfaces, and were more numerous than in the plane strain regions. The regions of IGC and LVC were larger and more more numerous for the T-L orientation specimens from both the near-surface and mid-plane locations, which would be consistent with the overall grain morphology observed. No correlation was observed between the occurrences of LVC and IGC and the K_{JIci} and T_R values.

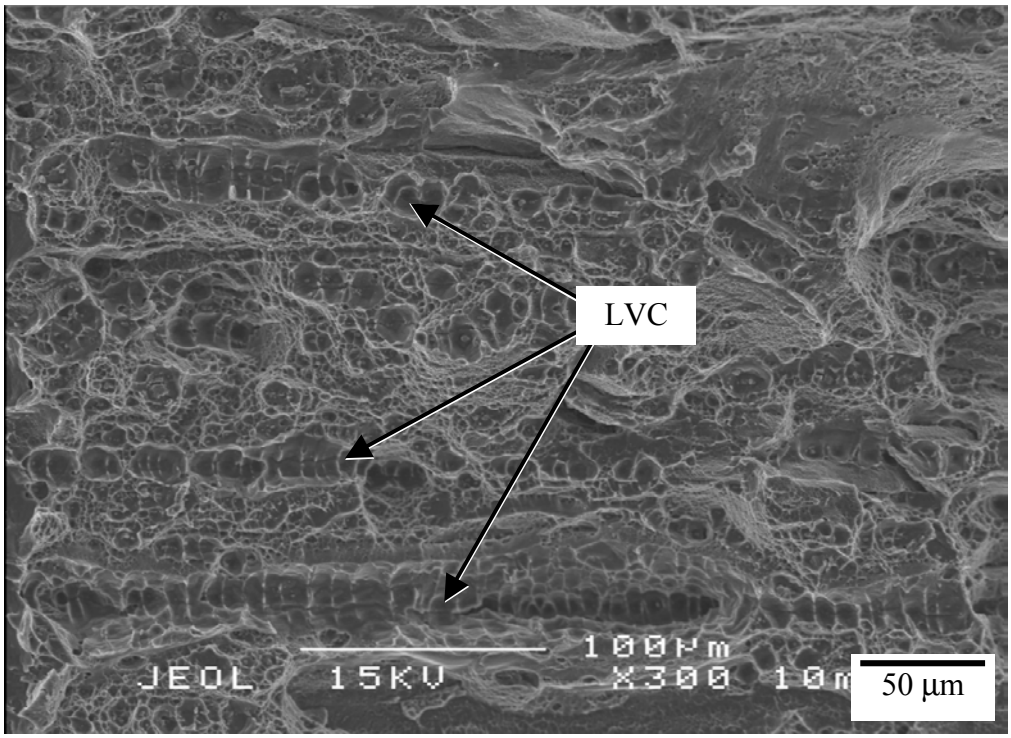

Figure 27. Typical appearance of regions of linear void coalescence (LVC).

Microscopically, the predominant fracture mode for all specimens was ductile transgranular microvoid coalescence (TGMVC), both in the plane strain and plane stress regions (Figure 29). Void-initiating particles were non-uniformly distributed across the fracture surfaces and were primarily $\leq 2\mu m$ in diameter. The non-uniform distribution of particles and growth of individual microvoids produced a bimodal distribution of very large and very small dimples, as illustrated in Figure 29(a). In general the dimples were equiaxed and were bounded by a lip or rim that is consistent with uniaxial tensile loading [24]. The large dimples were typically associated with void initiation at particle clusters, as shown in Figure 29(b), while the smaller dimples were associated with individual particles. Apparent void sheets (VS) were observed on all fracture surfaces, appearing as regions of very fine dimples often at angles to the fracture surface, as shown in Figure 29(c). Fracture of ligaments between regions of TGMVC occurs by the formation and coalescence of fine secondary voids. An occasional larger particle, ranging from 5-20 µm, was also observed, and appeared to have fractured during specimen failure, as shown in Figure 29(c).

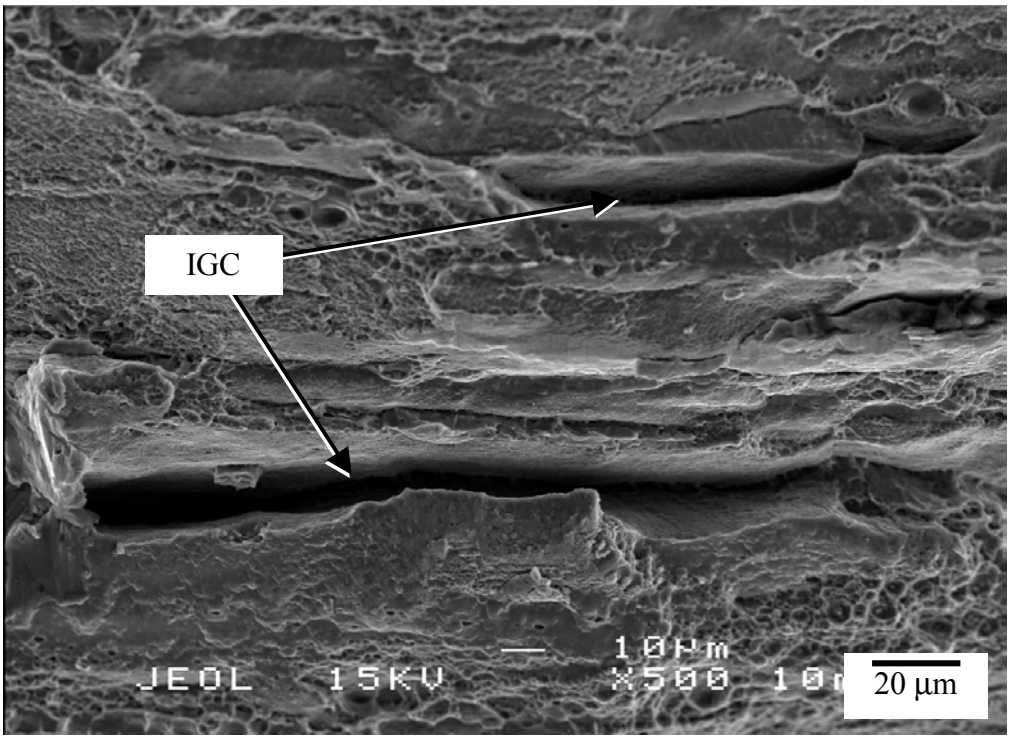

(a) Intergranular cracking (IGC).

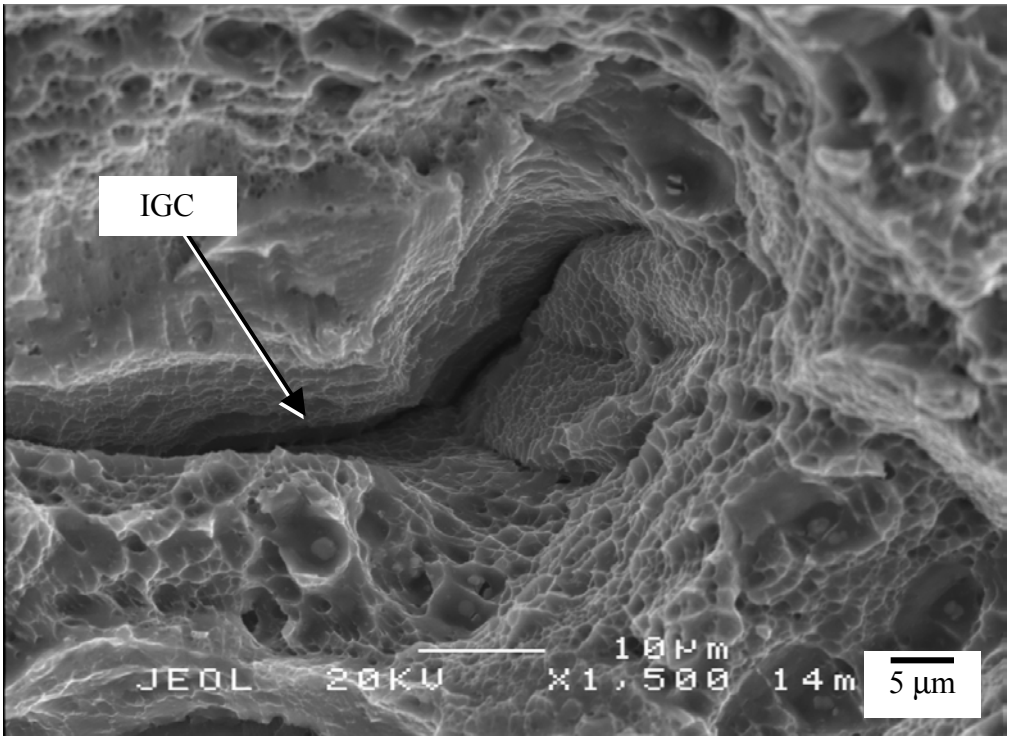

(b) Ductile dimples observed on intergranular facets.

Figure 28. Typical appearance of intergranular cracking (IGC).

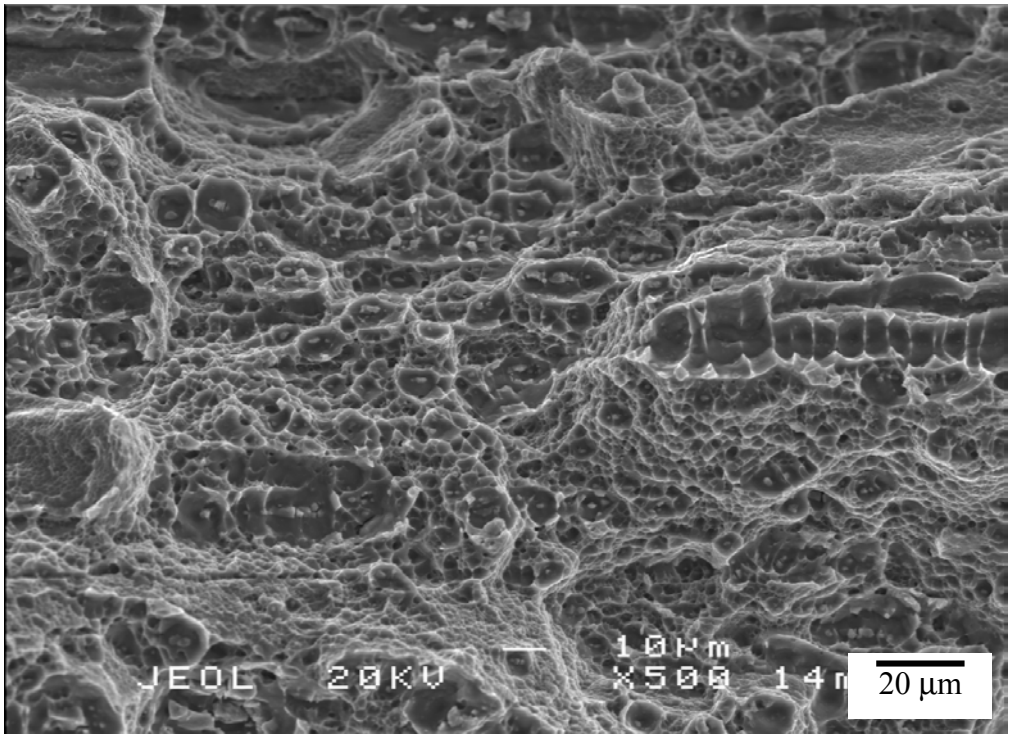

(a) Typical transgranular microvoid coalescence (TGMVC).

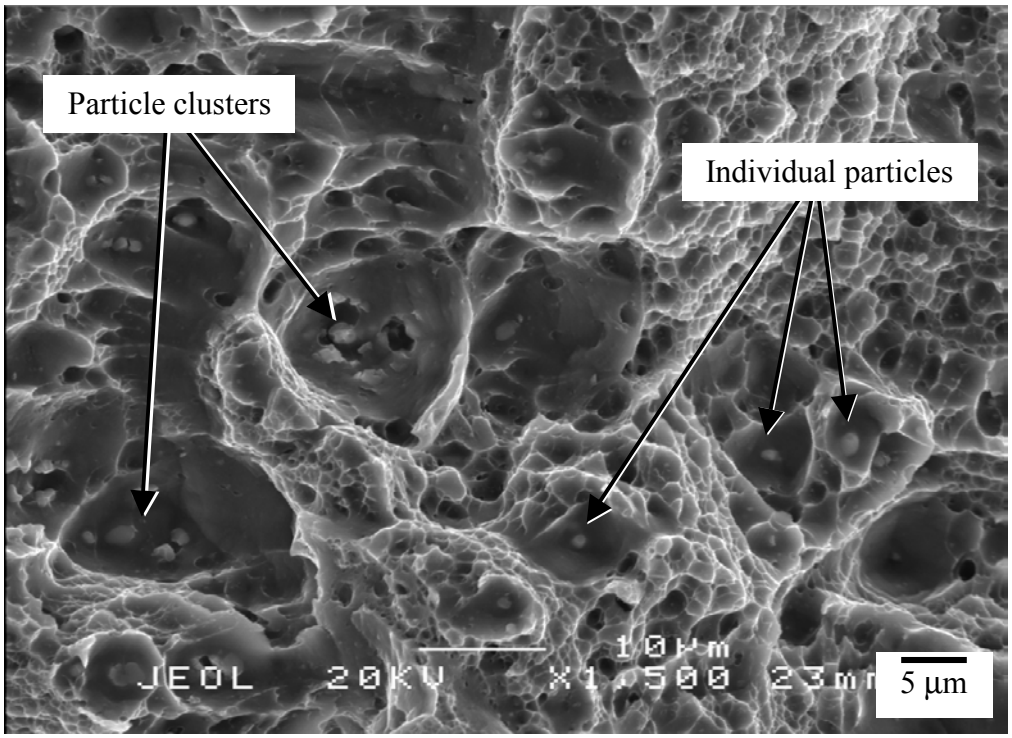

(b) Typical distribution of dimple size and void initiating particles

Figure 29. Microscopic fracture morphology observed for RX226-T8 plate.

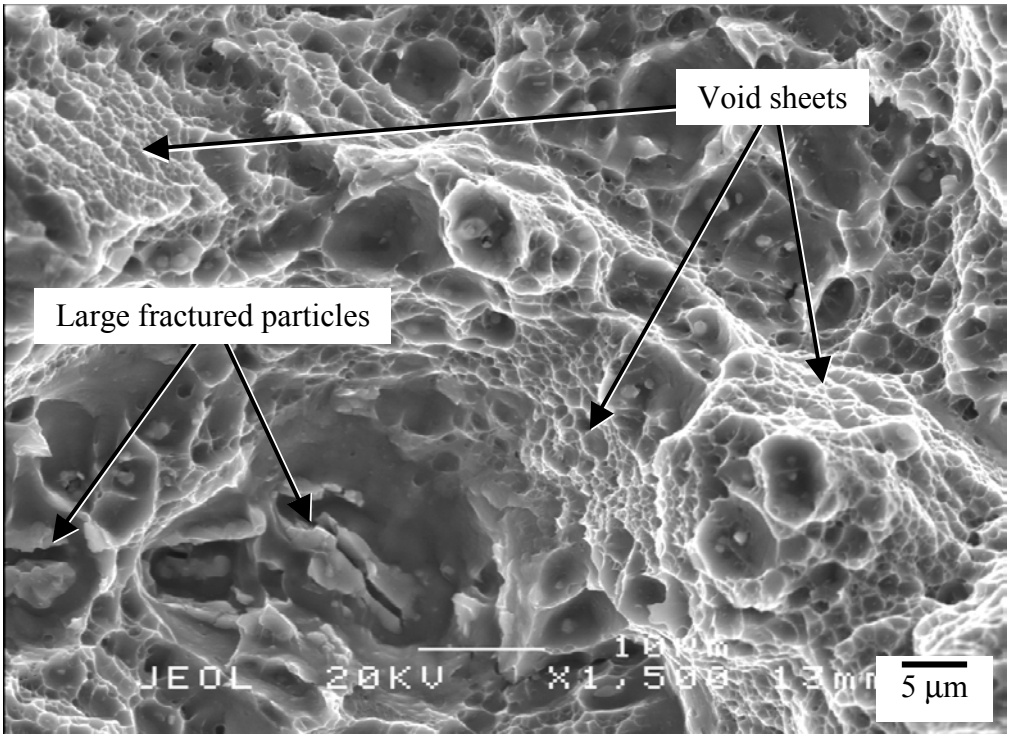

(c) Typical appearance of void sheets.

Figure 29. concluded.

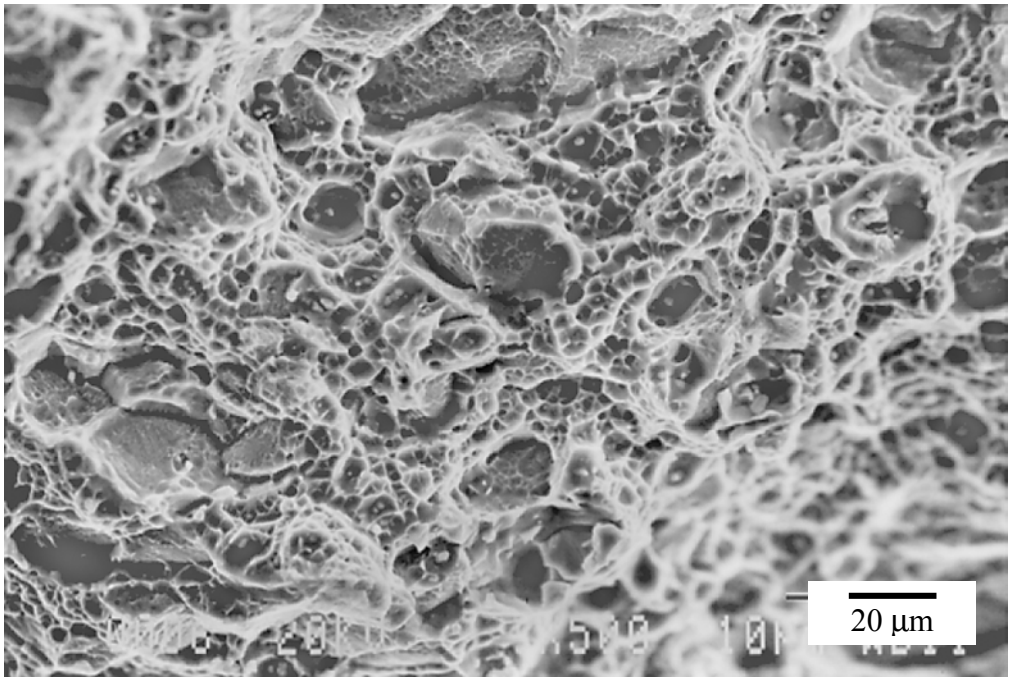

Figure 30. Typical TGMVC fracture morphology observed for C415-T8 and C416-T8 sheet.

The fracture morphology of alloys C415 and C416 was TGMVC linked by void sheets. Fracture surfaces exhibited dimples associated with second phase particles that were uniformly distributed throughout the grain structure. As shown in Figure 30, a small fraction of intergranular fracture was also evident, which was likely associated with grain boundary particle decoration. However, LVC was not observed for C415 and C416. The occurrence of LVC in RX226, resulting from the highly elongated grain morphology and tendency for linear arrays of grain boundary particles, likely contributed to lower fracture toughness values compared to C415 and C416. The lower toughness may also be associated with non-optimized material processing for the laboratory produced RX226-T8 plate.

Summary and Conclusions

The potential of Al-Cu-Mg-Ag alloy RX226 for application to integrally stiffened airframe structure was assessed through evaluation of the microstructure and mechanical properties of RX226-T8 plates. Property uniformity was evaluated as a function of plate thickness location and orientation, and the results were compared with sheet gage materials, C415 and C416, which have similar chemistry. Specific findings include:

1) In general, the microstructures of the 0.5-inch, 1.0-inch, and 1.5-inch thick RX226-T8 plates were similar and exhibited pancake-shaped grain morphology that was predominantly recrystallized with weak texture components. The microstructures were generally homogenous through the thickness, with the exception of a narrow band of smaller, more equiaxed grains near the surfaces of the 0.5-inch and 1.0-inch thick plates.

2) Yield and ultimate tensile strengths of 1.0-inch thick RX226-T8 plate were relatively isotropic as a function of both orientation and thickness location and were within 5% of values for commercially produced C415-T8 and C416-T8 sheet.

3) Initiation fracture toughness, K_{JIci}, of the 1.0-inch thick RX226-T8 plate was 15% (longitudinal) to 35% (transverse) lower than values for C415-T8 and C416-T8 sheet. Anisotropy in both K_{JIci} and tearing modulus, T_R, parameters was somewhat higher for the RX226 plate when compare to values for C415 and C416 sheet. This may be related to the non-uniform size and distribution of second phase particles present, the highly elongated grain morphology, and the resulting linear arrays of grain boundary particles observed in the RX226-T8 plate.

4) The fracture mode of the RX226-T8 plate was ductile transgranular microvoid coalescence for both orientations and through-thickness plate locations. Intergranular cracking and regions of linear void coalescence were observed on all fracture surfaces but were noticeably larger for the T-L orientation.

In conclusion, the RX226-T8 plate evaluated is a promising material for application as machined integrally stiffened structure. The uniform grain structure and low anisotropy in mechanical properties suggest that uniform properties could be expected in a fully machined structure. While the strength-toughness combination for the RX226-T8 plate was lower than that of C415-T8 and C416-T8 sheet, it is anticipated that improvements in chemistry and thermomechanical processing should result in increased strength and toughness properties while minimizing second phase particles.

References

1. Starke, E. A., Jr.: NASA-UVa Light Aerospace Alloy and Structure Technology Program Supplement: Aluminum-Based Materials for High Speed Aircraft. NASA/CR-97-206248, December 1997, pp. 1-99.

2. Chellman, D.; Cornell, B.; Bayha, T.; Schlosberg, R.; and Yaney, D.: Aluminum Development Technology - Materials Research for High Speed Civil Transport. Final Report for Contract No. NAS1-20015, Task 2, Period of Performance January 1994 to December 1995, LMAS Report No. LG96ER0144, November 1996.

3. Domack, M. S.; Dicus, D. L.; Edahl, R. A.; and Chellman, D. J.: Effect of Thermal Exposure on the Strength-Toughness Behavior of Elevated Temperature Service Aluminum Alloys. The 6th International Conference on Aluminum Alloys (ICAA-6), Toyohashi, Japan, July 5-10, 1998, pp. 1081-1086.

4. Beffort, O.; Solenthaler, C.; and Speidel, M. O.: Improvement of Strength and Fracture Toughness of a Spray-deposited Al-Cu-Mg-Ag-Mn-Ti-Zr Alloy by Optimized Heat Treatments and Thermomechanical Treatments. Materials Science and Engineering, A191, 1995, pp. 113-120.

5. Munroe, J.; Wilkins, K.; Gruber, M.: Integral Airframe Structures (IAS) – Validated Feasibility Study of Integrally Stiffened Metallic Fuselage Panels for Reducing Manufacturing Costs. NASA/CR-2000-209337, May 2000.

6. ASTM E8-01 - Standard Test Methods for Tension Testing of Metallic Materials. Annual Book of ASTM Standards, Vol. 3.0.1, American Society for Testing and Materials, Philadelphia, PA, 2002.

7. ASTM E1820-01 - Standard Test Methods for Measurement of Fracture Toughness. Annual Book of ASTM Standards, Vol. 3.0.1, American Society for Testing and Materials, Philadelphia, PA, 2002.

8. Donald, J. K.; and Ruschau, J.: Direct Current Potential Difference Fatigue Crack Measurement Techniques. Fatigue Crack Measurement: Techniques and Applications, K. J. Marsh, R. O. Ritchie, Eds., EMAS, West Midlands, UK, 1991, pp. 11-37.

9. Baker, A.: A DC Potential Drop Procedure for Crack Initiation and R-Curve Measurements During Ductile Fracture Tests. Elastic-Plastic Fracture Test Methods: The User's Experience, ASTM STP 856, E. T. Wessel and F. J. Loss, Eds., American Society for Testing and Materials, Philadelphia, PA, 1985, pp. 394-410.

10. Schwalbe, K-H; Hellman, D.; Heerens, J.; Knaack, J.; and Muller-Roos, J.: Measurement of Stable Crack Growth Including Detection of Initiation of Growth Using the DC Potenial Drop and the Partial Unloading Methods. Elastic-Plastic Fracture Test Methods: The User's Experience, ASTM STP 856, E. T. Wessel and F. J. Loss, Eds., American Society for Testing and Materials, Philadelphia, PA, 1985, pp. 338-362.

11. Paris, P. C.; Tada H.; Zahoor, A.; and Ernst H.: The Theory of Instability of the Tearing Mode of Elastic-Plastic Crack Growth. Elastic-Plastic Fracture, ASTM STP 668, J. D. Landes, J. A. Begley, and G. A. Clarke, Eds., American Society for Testing and Materials, Philadelphia, PA, 1979, pp. 5-36.

12. Mondolfo, L. F.: Aluminum Alloys Structure and Properties, Woburn, MA: Butterworth and Co., 1976, pp. 81-86.

13. Aluminum: Properties and Physical Metallurgy, Hatch, J. E, Ed., American Society for Metals, 1984, pp. 119-125.

14. Reynolds, A. P.; and R. E. Crooks, R. E.: The Effect of Thermal Exposure on the Fracture Behavior of Aluminum Alloys Intended for Elevated Temperature Service. Elevated Temperature Effects on Fatigue and Fracture, ASTM STP 1297, R. S. Piascik, R. P. Gangloff, and A. Saxena, Eds, American Society for Testing and Materials, 1997, pp. 191-205.

15. Reynolds, A. P.; and Li, Q.: The Effect of Elevated Temperature on Fracture Reistance and Fracture Path in a Precipitation Strengthened Aluminum Alloy. Scripta Materialia, Vol. 34, No. 11, 1996, pp. 1803-1808.

16. Cassada, W. A.; and Bartholomeusz, M. F.: The Effect of Cu and Mg Content on Mechanical Properties of Al-Cu-Mg Alloys With and Without Ag Additions. Materials Science Forum, Vols. 217-222, 1996, pp. 1765-1770.

17. Polmear, I. J.: Role of Trace Elements in Aged Aluminum Alloys, Mater. Sci. Forum, 13, 1987, pp. 195-214.

18. Stanley, J. T.: Microstructure and Toughness of High-strength Aluminum Alloys. Properties Related to Fracture Toughness. ASTM STP 605, American Society for Testing and Materials, Montreal Canada, June 22-27, 1975, pp. 71-98.

19. Stanley, J. T.: Influence of Microstructure on Fatigue and Fracture of Aluminum Alloys, Aluminum, 55, 1979, pp. 277-281.

20. Stanley, J. T.; Truckner, W. G.; Bucci, R. J.; and Thakker, A. B.: Improving Fracture Toughness of Aluminum Aircraft Alloys, Aluminum, 53, 1977, pp. 667-669.

21. Haynes, M. J.; Sommerday, B. P.; Lach, C. L.; and Gangloff, R. P.: Micromechanical Modeling of Temperature-Dependent Initiation Fracture Toughness in Advanced Aluminum Alloys. Elevated Temperature Effects on Fatigue and Fracture, ASTM STP 1297, R. S. Piascik, R.P Gangloff, and A. Saxena, eds., American Society for Testing and Materials, 1997, pp. 165-190.

22. Haynes, M. J.; and Gangloff, R. P.: High Resolution R-Curve Characterization of the Fracture Toughness of Thin Sheet Aluminum Alloys. Journal of Testing and Evaluation, 1997, pp. 82-98.

23. Jata, K. V.; Vasudevan, A. K.: Effect of fabrication and microstructure on the fracture initiation and growth toughness of Al-Li-Cu alloys. Mat. Sci. and Eng., A241, 1998, pp. 104-113.

24. McDonnell-Douglas Astronautics Company, Huntington Beach, CA. "SEM/TEM Fractography Handbook", (MCIC HB06) Columbus, OH: Metals and Ceramic Information Center, December, 1975, pp. 25-57.

REPORT DOCUMENTATION PAGE

Form Approved
OMB No. 0704-0188

1. REPORT DATE *(DD-MM-YYYY)*	2. REPORT TYPE	3. DATES COVERED *(From - To)*
01- 08 - 2003	Technical Memorandum	

4. TITLE AND SUBTITLE
Characterization of Al-Cu-Mg-Ag Alloy RX226-T8 Plate

5a. CONTRACT NUMBER

5b. GRANT NUMBER

5c. PROGRAM ELEMENT NUMBER

6. AUTHOR(S)
Lach, Cynthia L.; Domack, Marcia S.

5d. PROJECT NUMBER

5e. TASK NUMBER

5f. WORK UNIT NUMBER
703-63-61-01-00

7. PERFORMING ORGANIZATION NAME(S) AND ADDRESS(ES)
NASA Langley Research Center
Hampton, VA 23681-2199

8. PERFORMING ORGANIZATION REPORT NUMBER
L-18313

9. SPONSORING/MONITORING AGENCY NAME(S) AND ADDRESS(ES)
National Aeronautics and Space Administration
Washington, DC 20546-0001

10. SPONSOR/MONITOR'S ACRONYM(S)
NASA

11. SPONSOR/MONITOR'S REPORT NUMBER(S)
NASA/TM-2003-212639

12. DISTRIBUTION/AVAILABILITY STATEMENT
Unclassified - Unlimited
Subject Category 26
Availability: NASA CASI (301) 621-0390 Distribution: Standard

13. SUPPLEMENTARY NOTES
An electronic version can be found at http://techreports.larc.nasa.gov/ltrs/ or http://ntrs.nasa.gov

14. ABSTRACT

Aluminum-copper-magnesium-silver (Al-Cu-Mg-Ag) alloys that were developed for thermal stability also offer attractive ambient temperature strength-toughness combinations, and should therefore be considered for a broad range of airframe structural applications. The current study evaluated the alloy RX226-T8 in plate gages and compared performance with sheet gage alloys of similar composition. Tensile properties, plane strain fracture toughness, and plane stress tearing resistance were examined as a function of orientation at two thickness locations in the plate, near the surface and at the mid-plane. Tensile strengths were relatively isotropic, with variations in yield and tensile strengths of less than 2% as a function of orientation and plate thickness location. Ductility and fracture toughness varied by more than 15% with orientation. Tensile strengths were within 5% of values for commercial sheet but fracture toughness was more than 16% lower. The microstructure of the RX226-T8 plate was predominantly recrystallized with weak texture and was uniform through the plate with the exception of a fine-grained layer near the surface. Second phase particles were located on grain boundaries aligned parallel to the rolling direction. Examination of the fracture surfaces of the toughness specimens revealed that fracture occurred predominantly by transgranular microvoid coalescence.

15. SUBJECT TERMS
Al-Cu-Ag-Mg alloys; RX226-T8; Tensile properties; Fracture properties; SEM; Mechanical properties; Transgranular microvoid coalescence

16. SECURITY CLASSIFICATION OF:			17. LIMITATION OF ABSTRACT	18. NUMBER OF PAGES	19a. NAME OF RESPONSIBLE PERSON
a. REPORT	b. ABSTRACT	c. THIS PAGE			STI Help Desk (email: help@sti.nasa.gov)
					19b. TELEPHONE NUMBER *(Include area code)*
U	U	U	UU	45	(301) 621-0390